

A MULTILEVEL BLOCK PRECONDITIONER FOR THE HDG TRACE SYSTEM APPLIED TO INCOMPRESSIBLE RESISTIVE MHD

SRIRAMKRISHNAN MURALIKRISHNAN*, STEPHEN SHANNON†, TAN BUI-THANH‡,
AND JOHN N. SHADID§

Abstract. We present a scalable block preconditioning strategy for the trace system coming from the high-order hybridized discontinuous Galerkin (HDG) discretization of incompressible resistive magnetohydrodynamics (MHD). We construct the block preconditioner with a least squares commutator (BFBT) approximation for the inverse of the Schur complement that segregates out the pressure unknowns of the trace system. The remaining velocity, magnetic field, and Lagrange multiplier unknowns form a coupled nodal unknown block (the upper block), for which a system algebraic multigrid (AMG) is used for the approximate inverse. The complexity of the MHD equations together with the algebraic nature of the statically condensed HDG trace system makes the choice of smoother in the system AMG part critical for the convergence and performance of the block preconditioner. Our numerical experiments show GMRES preconditioned by ILU(0) of overlap zero as a smoother inside system AMG performs best in terms of robustness, time per nonlinear iteration and memory requirements. With several transient test cases in 2D and 3D including the island coalescence problem at high Lundquist number we demonstrate the robustness and parallel scalability of the block preconditioner. Additionally for the upper block a preliminary study of an alternate nodal block system solver based on a multilevel approximate nested dissection is presented. On a 2D island coalescence problem the multilevel approximate nested dissection preconditioner shows better scalability with respect to mesh refinement than the system AMG, but is relatively less robust with respect to Lundquist number scaling.

Key words. Block preconditioners, BFBT, HDG, High-Order, MHD, AMG, Multilevel

AMS subject classifications. 65N30, 65N55, 65N22, 65N12, 65F10

1. Introduction. Incompressible visco-resistive magnetohydrodynamics (MHD) equations play an important role in modeling low Lundquist number liquid metal flows, high Lundquist number large-guide-field fusion plasmas and low flow-Mach-number compressible flows [6, 16, 36]. The mathematical basis for the continuum modeling of these systems is the solution of the governing partial differential equations (PDEs) describing conservation of mass, momentum, and energy, augmented by the low-frequency Maxwell's equations. The multiphysics phenomena produced by this strongly coupled nonlinear system includes, convective transport, momentum forces evolving from pressure gradients and Lorentz forces from the magnetic field, Alfvén wave propagation, and diffusion effects from the viscosity and resistivity of the plasma system. Additionally the coupling of the conservation equations to elliptic constraints from the incompressibility assumption and the solenoidal involution property of the magnetic field add significant complexity to the block structured interactions of the unknowns. Finally the resulting response of these systems is also characterized by a wide range of spatial and temporal scales which makes efficient solution of these

*Department of Aerospace Engineering and Engineering Mechanics, The University of Texas at Austin, Austin, TX 78712, USA. Current address: Paul Scherrer Institut, 5232 Villigen, Switzerland.

†Oden Institute for Computational Engineering and Sciences, The University of Texas at Austin, Austin, TX 78712, USA.

‡Department of Aerospace Engineering and Engineering Mechanics, and Oden Institute for Computational Engineering and Sciences, The University of Texas at Austin, Austin, TX 78712, USA.

§Computational Mathematics Department, Sandia National Laboratories, Albuquerque, NM87185 and Department of Mathematics and Statistics, University of New Mexico, Albuquerque, NM 87131.

systems extremely challenging. In the context of time integration of these systems some form of implicitness is required to deal with the infinite pressure wave speed and to remove one or more sources of stiffness arising from diffusion and fast-waves in the MHD system. The potential benefit of implicit methods however require robust, efficient and scalable nonlinear and linear iterative solvers/preconditioners which can handle the highly stiff algebraic systems generated from incompressible MHD equations.

Over the past few years there has been significant progress in the area of fully implicit robust and scalable MHD simulations as evidenced in [6, 9, 28, 36, 43] among others. However, these simulations use low-order stabilized FEM, mixed FEM or finite volume methods for the spatial discretization and hence require larger numbers of unknowns for high accuracy. They also have low computation to communication ratio which is not preferable for achieving high performance (in terms of percentage of peak performance) in modern extreme scale computing architectures.

High-order spatial discretizations are attractive in this context as they have high computation to communication ratio and can simulate the problem with a reduced number of unknowns compared to low-order discretizations for similar or higher accuracy. Hybridized discontinuous Galerkin (HDG) methods introduced a decade ago are promising candidates for high-order spatial discretization due to the following reasons. It combines the important advantages of DG methods namely arbitrary high-order with compact stencil, flux upwinding on element boundaries and the ability to handle complex geometries together with the smaller and sparser linear system which involves only trace unknowns, a characteristic of hybridized methods.

The first HDG method for incompressible resistive MHD equations is proposed in [20, 38] and very recently HDG methods for ideal and resistive compressible MHD equations are introduced in [7]. A current challenge in the context of high-order HDG discretizations of MHD is the availability of robust, efficient and scalable iterative solvers/preconditioners and that is the goal of our work. The availability of such a solver will enable large scale 3D high-order HDG simulations of MHD on realistic geometries and this will have large impact in many areas of plasma physics research including but not limited to nuclear fusion.

Towards that extent, we propose a block preconditioning strategy for trace systems [25] arising from HDG discretizations of incompressible resistive MHD [20]. Even though the concept of block preconditioning for saddle point systems has been studied by various researchers [3, 9, 11–13, 28, 29, 32, 41–43], it is mostly in the context of volume based low-order discretizations such as mixed FEM, stabilized FEM, finite volume and finite difference.

In this development the linear systems coming from HDG discretization of incompressible resistive MHD [20] pose several challenges which are as follows. First, it involves only trace unknowns which live on the skeleton of the mesh and moreover they all are not of the same nature. Second, since it is obtained after static condensation of the volume unknowns the linear system is mostly algebraic and it is non-trivial to identify the nature of different blocks in the linear system as opposed to linear systems coming from stabilized and mixed FEM. In [31, 39] block preconditioners for HDG discretization of Stokes and incompressible Navier Stokes equations are presented. However, the authors eliminated only velocity volume unknowns by static condensation and the final linear system contains velocity and pressure trace unknowns together with the pressure volume unknowns. To the best of our knowledge we are not aware of block preconditioners for HDG discretizations which completely eliminate all the

volume unknowns and solve the linear system with only trace unknowns and in that aspect our work is a first step towards it.

In this effort we employ the BFBT framework of block preconditioning first introduced in [12] for finite difference and finite element discretizations of incompressible Navier-Stokes equations. However, the novelty of our work lies in the careful choice of different components involved in the framework so that it leads to an effective preconditioner for HDG discretization of incompressible resistive MHD. We demonstrate this numerically by means of several 2D and 3D benchmark problems and a theoretical analysis of the current approach is left for future work.

This paper is organized as follows. In section 2, we introduce the notations which will be followed throughout the rest of the paper. We present the incompressible resistive MHD equations and the relevant non-dimensional parameters in section 3. Then in section 4, we present an HDG scheme for the discretization of the MHD system and identify the block structure in it. We then proceed to introduce a block preconditioning strategy for the linear system in section 5. Section 6 presents various 2D and 3D transient test cases to test the robustness and scalability of the block preconditioner. Finally in section 7 we discuss the conclusions and directions for future research.

2. Notation. In this section we introduce the common notations and conventions which will be followed in the rest of the paper. Let us partition $\Omega \in \mathbb{R}^d$, an open and bounded domain, into N_T nonoverlapping elements $T_j, j = 1, \dots, N_T$ with Lipschitz boundaries such that $\Omega_h := \cup_{j=1}^{N_T} T_j$ and $\bar{\Omega} = \bar{\Omega}_h$. Here, h is defined as $h := \max_{j \in \{1, \dots, N_T\}} \text{diam}(T_j)$. We denote the skeleton of the mesh by $\mathcal{E}_h := \cup_{j=1}^{N_T} \partial T_j$, the set of all (uniquely defined) interfaces e between elements. We conventionally identify \mathbf{n}^- as the outward normal vector on the boundary ∂T of element T (also denoted as T^-) and $\mathbf{n}^+ = -\mathbf{n}^-$ as the outward normal vector of the boundary of a neighboring element (also denoted as T^+). Furthermore, we use \mathbf{n} to denote either \mathbf{n}^- or \mathbf{n}^+ in an expression that is valid for both cases, and this convention is also used for other quantities (restricted) on a face $e \in \mathcal{E}_h$. For the sake of convenience, we denote by \mathcal{E}_h^∂ the set of all boundary faces on $\partial\Omega$, by $\mathcal{E}_h^\circ := \mathcal{E}_h \setminus \mathcal{E}_h^\partial$ the set of all interior faces, and $\partial\Omega_h := \{\partial T : T \in \Omega_h\}$.

For simplicity in writing we define $(\cdot, \cdot)_T$ as the L^2 -inner product on a domain $T \in \mathbb{R}^d$ and $\langle \cdot, \cdot \rangle_T$ as the L^2 -inner product on a domain T if $T \in \mathbb{R}^{d-1}$. We shall use $\|\cdot\|_T := \|\cdot\|_{L^2(T)}$ as the induced norm for both cases and the particular value of T in a context will indicate which inner product the norm is coming from. We also denote the ε -weighted norm of a function u as $\|u\|_{\varepsilon, T} := \|\sqrt{\varepsilon}u\|_T$ for any positive ε . Moreover, we define $(u, v)_{\Omega_h} := \sum_{T \in \Omega_h} (u, v)_T$ and $\langle u, v \rangle_{\mathcal{E}_h} := \sum_{e \in \mathcal{E}_h} \langle u, v \rangle_e$ whose induced (weighted) norms are clear, and hence their definitions are omitted. We shall use boldface lowercase letters, e.g. \mathbf{u} , for vector-valued functions and boldface uppercase letters, e.g. \mathbf{L} , for matrices and tensors. The notations of inner products and norms are naturally extended for these cases in a component-wise manner. We use the terms ‘‘skeletal unknowns’’ and ‘‘trace unknowns’’ interchangeably and they both refer to the unknowns on the mesh skeleton. They are denoted with hats to differentiate it from the corresponding volume unknowns.

We define the gradient of a vector, the divergence of a matrix, and the outer product symbol \otimes as:

$$(\nabla \mathbf{u})_{ij} = \frac{\partial u_i}{\partial x_j}, \quad (\nabla \cdot \mathbf{L})_i = \nabla \cdot \mathbf{L}(i, \cdot) = \sum_{j=1}^3 \frac{\partial L_{ij}}{\partial x_j}, \quad (\mathbf{a} \otimes \mathbf{b})_{ij} = a_i b_j = (\mathbf{a} \mathbf{b}^T)_{ij}.$$

We define $\mathcal{P}^p(T)$ as the space of polynomials of degree at most p on a domain T . Similarly, $\mathcal{P}^p(e)$ denotes the polynomials of degree at most p on the mesh skeleton edge e and the extensions to vector- or matrix-valued polynomials $[\mathcal{P}^p(T)]^d$, $[\mathcal{P}^p(T)]^{d \times d}$, $[\mathcal{P}^p(e)]^d$, etc, are straightforward. We define the ‘‘jump’’ operator for any quantity (\cdot) as $\llbracket (\cdot) \rrbracket := (\cdot)^- + (\cdot)^+$.

3. Incompressible visco-resistive MHD system. The visco-resistive, incompressible MHD equations in non-dimensional form are given by

$$\frac{\partial \mathbf{u}}{\partial t} + \mathbf{u} \cdot \nabla \mathbf{u} + \nabla q - \frac{1}{\text{Re}} \Delta \mathbf{u} - \kappa (\nabla \times \mathbf{b}) \times \mathbf{b} = \mathbf{f}, \quad (3.1a)$$

$$\nabla \cdot \mathbf{u} = 0, \quad (3.1b)$$

$$\kappa \frac{\partial \mathbf{b}}{\partial t} + \frac{\kappa}{\text{Rm}} \nabla \times (\nabla \times \mathbf{b}) - \kappa \nabla \times (\mathbf{u} \times \mathbf{b}) + \nabla r = \mathbf{g}, \quad (3.1c)$$

$$\nabla \cdot \mathbf{b} = 0. \quad (3.1d)$$

Here, \mathbf{u} is the fluid velocity field, \mathbf{b} is the magnetic field, q is the mechanical pressure and r denotes the Lagrange multiplier which is used to enforce the solenoidality of the magnetic field constraint [8, 36]. Thus allows the enforcement of the divergence-free constraint and at the same time it is just an auxiliary discrete variable because in essence we are solving for a variable that would be zero in the solution to the continuous problem. This can be seen by taking divergence of equation (3.1c) which gives $\Delta r = 0$ (assuming the magnetic source term \mathbf{g} to be divergence-free) and together with homogeneous Dirichlet boundary conditions gives $r = 0$. More details about this approach can be found in [8, 20, 34–36].

The non-dimensional parameters in (3.1) are as follows. $\text{Re} := \frac{\rho l_0 u_0}{\mu}$ is the fluid Reynolds number which measures the ratio of inertial forces to viscous forces, $\text{Rm} := \frac{\mu_0 u_0 l_0}{\eta}$ is the magnetic Reynolds number which is the ratio of magnetic advection to magnetic diffusion, $\kappa := \frac{b_0^2}{\rho \mu_0 u_0^2}$ is the coupling parameter and is the ratio of electromagnetic forces to inertial forces. Here, ρ is the fluid density, μ is the viscosity, μ_0 is the permeability of free space and η the resistivity. The characteristic length, velocity and magnetic scales are given by l_0 , u_0 and b_0 respectively. The parameters κ , Re and Rm are related by $\kappa = \frac{\text{Ha}^2}{\text{ReRm}}$, where $\text{Ha} := \frac{b_0 l_0}{\sqrt{\mu \eta}}$ is the Hartmann number. We can also write κ as $\kappa = \frac{u_A^2}{u_0^2}$, where $u_A := \frac{b_0}{\sqrt{\rho \mu_0}}$ is the Alfvén speed. If we choose the characteristic velocity as Alfvén speed then the resulting magnetic Reynolds number is referred as Lundquist number S . We refer the readers to [16, 24] for details on non-dimensional parameters in the MHD system.

We put (3.1) into first order form for discretizing with HDG and towards that end let us define the auxiliary variables \mathbf{L} and \mathbf{J} which represents the velocity gradient

and curl of magnetic field respectively. The first order system is given by

$$\text{Re}\mathbf{L} - \nabla\mathbf{u} = \mathbf{0}, \quad (3.2a)$$

$$\frac{\partial\mathbf{u}}{\partial t} + \nabla \cdot (\mathbf{u} \otimes \mathbf{u}) + \nabla q - \nabla \cdot \mathbf{L} - \kappa(\nabla \times \mathbf{b}) \times \mathbf{b} = \mathbf{f}, \quad (3.2b)$$

$$\nabla \cdot \mathbf{u} = 0, \quad (3.2c)$$

$$\frac{\text{Rm}}{\kappa}\mathbf{J} - \nabla \times \mathbf{b} = \mathbf{0}, \quad (3.2d)$$

$$\kappa \frac{\partial\mathbf{b}}{\partial t} + \nabla r - \kappa \nabla \times (\mathbf{u} \times \mathbf{b}) + \nabla \times \mathbf{J} = \mathbf{g}, \quad (3.2e)$$

$$\nabla \cdot \mathbf{b} = 0. \quad (3.2f)$$

We refer to \mathbf{J} as the current density or simply the current and it should be understood in a non-dimensional sense with the characteristic value defined by $J_0 = \frac{\text{Rm}}{\kappa} \frac{b_0}{\mu_0 t_0}$.

The MHD system (3.2) is equipped with the following set of initial conditions

$$\mathbf{u}(t=0) = \mathbf{u}_0, \quad \mathbf{b}(t=0) = \mathbf{b}_0. \quad (3.3)$$

We also need to specify boundary conditions for the fluid components, magnetic components and the Lagrange multiplier. Since it is not important for the current discussion we will defer this till section 6 where we specify these details for each numerical experiment separately.

We will use the Picard nonlinear solver in our study and hence we consider the HDG schemes posed on the (Picard) linearized version of (3.2) about a prescribed velocity \mathbf{w} and a prescribed magnetic field \mathbf{d} [8]:

$$\text{Re}\mathbf{L} - \nabla\mathbf{u} = \mathbf{0}, \quad (3.4a)$$

$$\frac{\partial\mathbf{u}}{\partial t} + \nabla \cdot (\mathbf{u} \otimes \mathbf{w}) + \nabla q - \nabla \cdot \mathbf{L} - \kappa(\nabla \times \mathbf{b}) \times \mathbf{d} = \mathbf{f}, \quad (3.4b)$$

$$\nabla \cdot \mathbf{u} = 0, \quad (3.4c)$$

$$\frac{\text{Rm}}{\kappa}\mathbf{J} - \nabla \times \mathbf{b} = \mathbf{0}, \quad (3.4d)$$

$$\kappa \frac{\partial\mathbf{b}}{\partial t} + \nabla r - \kappa \nabla \times (\mathbf{u} \times \mathbf{d}) + \nabla \times \mathbf{J} = \mathbf{g}, \quad (3.4e)$$

$$\nabla \cdot \mathbf{b} = 0. \quad (3.4f)$$

Here \mathbf{w} is assumed to reside in $H(\text{div}, \Omega)$ and be divergence-free, while \mathbf{d} is assumed to reside in $H(\text{div}, \Omega) \cap H(\text{curl}, \Omega)$.

4. HDG for incompressible MHD. In this section we present the HDG scheme first proposed in [20, 37].

Find $(\mathbf{L}, \mathbf{u}, q, \mathbf{J}, \mathbf{b}, r, \hat{\mathbf{u}}, \hat{\mathbf{b}}, \hat{r}, \rho)$ in $\mathbf{G}_h \times \mathbf{V}_h \times W_h \times \mathbf{H}_h \times \mathbf{C}_h \times S_h \times \widehat{\mathbf{V}}_h \times \widehat{\mathbf{C}}_h^t \times$

$\widehat{S}_h \times \mathcal{P}^0(\partial T)$ such that the local equations

$$\operatorname{Re}(\mathbf{L}, \mathbf{G})_T + (\mathbf{u}, \nabla \cdot \mathbf{G})_T - \langle \hat{\mathbf{u}}, \mathbf{G}\mathbf{n} \rangle_{\partial T} = 0, \quad (4.1a)$$

$$\begin{aligned} & \left(\frac{\partial \mathbf{u}}{\partial t}, \mathbf{v} \right)_T - (\nabla \cdot \mathbf{L}, \mathbf{v})_T + (\nabla q, \mathbf{v})_T - \frac{1}{2} (\mathbf{u} \otimes \mathbf{w}, \nabla \mathbf{v})_T + \frac{1}{2} (\nabla \mathbf{u}, \mathbf{v} \otimes \mathbf{w})_T \\ & + (\nabla \times \mathbf{b}, \mathbf{v} \times \kappa \mathbf{d})_T + \left\langle \frac{1}{2} (\mathbf{w} \cdot \mathbf{n}) \hat{\mathbf{u}} + \mathbf{S}_u (\mathbf{u} - \hat{\mathbf{u}}), \mathbf{v} \right\rangle_{\partial T} \\ & - [1 - \xi] \left\langle \mathbf{n} \times (\mathbf{b}^t - \widehat{\mathbf{b}}^t), \mathbf{v} \times \kappa \mathbf{d} \right\rangle_{\partial T} = (\mathbf{f}, \mathbf{v})_T, \end{aligned} \quad (4.1b)$$

$$- (\mathbf{u}, \nabla w)_T + \langle \hat{\mathbf{u}} \cdot \mathbf{n}, w - \bar{w} \rangle_{\partial T} + \langle \bar{q} - \rho, \bar{w} \rangle_{\partial T} = 0, \quad (4.1c)$$

$$\frac{\operatorname{Rm}}{\kappa} (\mathbf{J}, \mathbf{H})_T - (\mathbf{b}, \nabla \times \mathbf{H})_T - \left\langle \mathbf{n} \times \widehat{\mathbf{b}}^t, \mathbf{H} \right\rangle_{\partial T} = 0, \quad (4.1d)$$

$$\begin{aligned} & \kappa \left(\frac{\partial \mathbf{b}}{\partial t}, \mathbf{c} \right)_T + (\nabla \times \mathbf{J}, \mathbf{c})_T - (r, \nabla \cdot \mathbf{c})_T - (\mathbf{u} \times \kappa \mathbf{d}, \nabla \times \mathbf{c})_T + \langle \widehat{r}, \mathbf{c} \cdot \mathbf{n} \rangle_{\partial T} \\ & + \langle ([1 - \xi] \mathbf{u} + \xi \hat{\mathbf{u}}) \times \kappa \mathbf{d}, \mathbf{n} \times \mathbf{c} \rangle_{\partial T} + \left\langle \beta_t (\mathbf{b}^t - \widehat{\mathbf{b}}^t), \mathbf{c} \right\rangle_{\partial T} = (\mathbf{g}, \mathbf{c})_T, \end{aligned} \quad (4.1e)$$

$$(\nabla \cdot \mathbf{b}, s)_T + \left\langle \frac{1}{\beta_n} (r - \widehat{r}), s \right\rangle_{\partial T} = 0, \quad (4.1f)$$

the conservation equations

$$- \left\langle \llbracket -\mathbf{L}\mathbf{n} + q\mathbf{n} + \frac{1}{2} (\mathbf{w} \cdot \mathbf{n}) \mathbf{u} + \mathbf{S}_u (\mathbf{u} - \hat{\mathbf{u}}) + \kappa \mathbf{d} \times (\mathbf{n} \times \xi \mathbf{b}) \rrbracket, \widehat{\mathbf{v}} \right\rangle_e = 0, \quad (4.1g)$$

$$- \left\langle \llbracket \mathbf{n} \times \mathbf{J} + \beta_t (\mathbf{b}^t - \widehat{\mathbf{b}}^t) - \mathbf{n} \times ([1 - \xi] \mathbf{u} \times \kappa \mathbf{d}) \rrbracket, \widehat{\mathbf{c}}^t \right\rangle_e = 0, \quad (4.1h)$$

$$- \left\langle \llbracket \mathbf{b} \cdot \mathbf{n} + \frac{1}{\beta_n} (r - \widehat{r}) \rrbracket, \widehat{s} \right\rangle_e = 0, \quad (4.1i)$$

and the additional constraint

$$\langle \hat{\mathbf{u}} \cdot \mathbf{n}, \psi \rangle_{\partial T} = 0 \quad (4.1j)$$

hold for all $(\mathbf{G}, \mathbf{v}, w, \mathbf{H}, \mathbf{c}, s, \widehat{\mathbf{v}}, \widehat{\mathbf{c}}^t, \widehat{s}, \psi)$ in $\mathbf{G}_h \times \mathbf{V}_h \times W_h \times \mathbf{H}_h \times \mathbf{C}_h \times S_h \times \widehat{\mathbf{V}}_h \times \widehat{\mathbf{C}}_h^t \times \widehat{S}_h \times \mathcal{P}^0(\partial T)$. In addition the pressure is subject to the constraint

$$(q, 1)_{\Omega_h} = 0.$$

In the above, the notation \bar{q} is defined by $\bar{q} := |\partial T|^{-1} \langle q, 1 \rangle_{\partial T}$ as the ∂T -wise average of q , and $|\partial T|$ is the length of the perimeter of element T . The new unknowns ρ which are sought in $\mathcal{P}^0(\partial T)$ represent the ∂T -wise or edge average pressure. Also, $\widehat{\mathbf{b}}^t$ represents the skeletal unknowns corresponding to the tangent magnetic field.

Here, the volume spaces are defined as

$$\mathbf{G}_h := \left\{ \mathbf{G} \in [L^2(\Omega_h)]^{d \times d} : \mathbf{G}|_T \in [\mathcal{P}^p(T)]^{d \times d}, \forall T \in \Omega_h \right\}, \quad (4.2a)$$

$$\mathbf{V}_h := \left\{ \mathbf{v} \in [L^2(\Omega_h)]^d : \mathbf{v}|_T \in [\mathcal{P}^p(T)]^d, \forall T \in \Omega_h \right\}, \quad (4.2b)$$

$$W_h := \left\{ w \in L^2(\Omega_h) : w|_T \in \mathcal{P}^p(T), \forall T \in \Omega_h \right\}, \quad (4.2c)$$

$$\mathbf{H}_h := \left\{ \mathbf{H} \in [L^2(\Omega_h)]^{\tilde{d}} : \mathbf{H}|_T \in [\mathcal{P}^p(T)]^{\tilde{d}}, \forall T \in \Omega_h \right\}, \quad (4.2d)$$

$$\mathbf{C}_h := \left\{ \mathbf{c} \in [L^2(\Omega_h)]^d : \mathbf{c}|_T \in [\mathcal{P}^p(T)]^d, \forall T \in \Omega_h \right\}, \quad (4.2e)$$

$$S_h := \left\{ s \in L^2(\Omega_h) : s|_T \in \mathcal{P}^p(T), \forall T \in \Omega_h \right\}, \quad (4.2f)$$

where \tilde{d} takes the value of one for 2D and three for 3D. We define the skeletal spaces as follows,

$$\widehat{\mathbf{V}}_h := \left\{ \widehat{\mathbf{v}} \in [L^2(\mathcal{E}_h)]^d : \widehat{\mathbf{v}}|_e \in [\mathcal{P}^p(e)]^d, \forall e \in \mathcal{E}_h \right\}, \quad (4.3)$$

$$\widehat{\mathbf{C}}_h^t := \left\{ \widehat{\mathbf{c}}^t \in [L^2(\mathcal{E}_h)]^{d-1} : \widehat{\mathbf{c}}^t|_e \in \widehat{\mathbf{C}}_h^t(e) \right\}, \quad (4.4)$$

$$\widehat{S}_h := \left\{ \widehat{s} \in L^2(\mathcal{E}_h) : \widehat{s}|_e \in \mathcal{P}^p(e), \forall e \in \mathcal{E}_h \right\}. \quad (4.5)$$

Here $\widehat{\mathbf{C}}_h^t(e)$ is a vector valued polynomial space with no normal component, defined by

$$\widehat{\mathbf{C}}_h^t(e) = \left\{ \sum_{i=1}^{d-1} \mathbf{t}^i \widehat{c}_{h,i} : \widehat{c}_{h,i} \in \mathcal{P}^p(e), \forall e \in \mathcal{E}_h \right\}, \quad (4.6)$$

where \mathbf{t}^i are tangent vectors to e . The values $\xi = \frac{1}{2}$, $\beta_n = \beta_t = 1$ are chosen and the stabilization \mathbf{S}_u is taken as

$$\mathbf{S}_u := \tau_t \mathbf{T} + \tau_n \mathbf{N}, \quad (4.7)$$

where $\mathbf{N} := \mathbf{n} \otimes \mathbf{n}$, $\mathbf{T} := -\mathbf{n} \times (\mathbf{n} \times \cdot) = \mathbf{I} - \mathbf{N}$, $\tau_t = \frac{1}{2} \sqrt{4 + (\mathbf{w} \cdot \mathbf{n})^2}$ and $\tau_n = \frac{1}{2} \sqrt{8 + (\mathbf{w} \cdot \mathbf{n})^2}$.

The well-posedness of the local and global solvers of the scheme (4.1) and also the error analysis is shown in [20, 37]. For this scheme the volume velocity and magnetic fields converge optimally as $\mathcal{O}(h^{p+1})$, whereas all the other volume variables converge as $\mathcal{O}(h^{p+1/2})$. The verification of this scheme for a number of prototypical MHD problems is shown in [20, 37].

After discretizing the time derivative terms in equation (4.1) by means of some time discretization scheme e.g., backward Euler, for each nonlinear iteration of Picard we need to solve a linear system. To that extent, we express the volume unknowns in terms of the skeletal unknowns through the local solvers, then we use the conservation conditions to generate the global linear system which has the following block form [37]

$$\begin{bmatrix} A & -D^\top & E & G \\ D & 0 & 0 & 0 \\ F & 0 & C & J \\ H & 0 & K & L \end{bmatrix} \begin{bmatrix} \widehat{U} \\ \rho \\ \widehat{B}^t \\ \widehat{R} \end{bmatrix} = \begin{bmatrix} F_1 \\ F_2 \\ F_3 \\ F_4 \end{bmatrix}. \quad (4.8)$$

We will use this block structure and develop a preconditioning strategy as shown in the next section.

5. A block preconditioner for the linear system. Before moving into the construction of the block preconditioner we first briefly explain the need for it in this case. If we want to precondition the linear system (4.8) using multigrid or multilevel methods, we cannot apply it directly because of the difference in the nature of the trace unknowns. The unknowns $(\widehat{U}, \widehat{B}^t, \widehat{R})$ are all nodal skeletal unknowns belonging to $\mathcal{P}^p(e)$, whereas the edge average pressure ρ is an element-wise constant and is independent of the solution order p . Thus with standard multigrid or multilevel methods, coarsening becomes an issue unless different strategies are employed for the different types of trace unknowns. This problem is also encountered in the linear systems arising from mixed finite element methods and a strategy to tackle this issue is block preconditioning. The idea is to identify and group blocks corresponding to different unknowns and use approximate block inverses for preconditioning [9, 11–13, 28, 32, 43]. Here we use similar techniques to develop a preconditioner for the linear system (4.8).

Towards this goal we first rewrite equation (4.8) into the saddle point form as follows

$$\begin{bmatrix} A & E & G & -D^\top \\ F & C & J & 0 \\ H & K & L & 0 \\ D & 0 & 0 & 0 \end{bmatrix} \begin{bmatrix} \widehat{U} \\ \widehat{B}^t \\ \widehat{R} \\ \rho \end{bmatrix} = \begin{bmatrix} F_1 \\ F_3 \\ F_4 \\ F_2 \end{bmatrix}. \quad (5.1)$$

Denoting the 3×3 block corresponding to the unknowns $(\widehat{U}, \widehat{B}^t, \widehat{R})$ as \mathcal{F} and $[D \ 0 \ 0]$ as \mathcal{B} we can write the above matrix as

$$\begin{bmatrix} \mathcal{F} & -\mathcal{B}^\top \\ \mathcal{B} & 0 \end{bmatrix}. \quad (5.2)$$

For a 2×2 block matrix such as (5.2) its block inverse (assuming \mathcal{F}^{-1} and \mathcal{S}^{-1} exists) can be written as [40]

$$\begin{bmatrix} \mathcal{F} & -\mathcal{B}^\top \\ \mathcal{B} & 0 \end{bmatrix}^{-1} = \begin{bmatrix} \mathcal{F}^{-1} & \mathcal{F}^{-1}\mathcal{B}^\top\mathcal{S}^{-1} \\ 0 & \mathcal{S}^{-1} \end{bmatrix} \begin{bmatrix} I & 0 \\ -\mathcal{B}\mathcal{F}^{-1} & I \end{bmatrix}, \quad (5.3)$$

where $\mathcal{S} := \mathcal{B}\mathcal{F}^{-1}\mathcal{B}^\top$ is the Schur complement. Now, when we use the block upper triangular matrix of the inverse (5.3) as a right preconditioner for the saddle point matrix (5.2) we get

$$\begin{bmatrix} \mathcal{F} & -\mathcal{B}^\top \\ \mathcal{B} & 0 \end{bmatrix} \begin{bmatrix} \mathcal{F}^{-1} & \mathcal{F}^{-1}\mathcal{B}^\top\mathcal{S}^{-1} \\ 0 & \mathcal{S}^{-1} \end{bmatrix} = \begin{bmatrix} I & 0 \\ \mathcal{B}\mathcal{F}^{-1} & I \end{bmatrix}. \quad (5.4)$$

All the eigenvalues of the preconditioned matrix have the value 1, and hence with a Krylov subspace method such as GMRES at most two iterations are needed to solve the system [11–13, 27].

However, the problem with this ideal preconditioner is that we need inverses of \mathcal{F} and \mathcal{S} which are expensive to compute. Hence a natural idea is to use approximations of these inverses in the construction of the preconditioner. First, let us consider the approximation for the inverse of the Schur complement matrix \mathcal{S} . We will follow the approach shown in [11–13] for incompressible Navier–Stokes equations to derive an approximation for the inverse of the Schur complement.

To that extent, if we can find an approximate commutator $\tilde{\mathcal{F}}$ such that

$$\mathcal{B}^\top \tilde{\mathcal{F}} \approx \mathcal{F} \mathcal{B}^\top, \quad (5.5)$$

then pre-multiplying by \mathcal{F}^{-1} and post-multiplying by $\tilde{\mathcal{F}}^{-1}$ (assuming both inverses exists) on both sides of the above equation we get

$$\mathcal{F}^{-1} \mathcal{B}^\top \approx \mathcal{B}^\top \tilde{\mathcal{F}}^{-1}. \quad (5.6)$$

Using (5.6) we can write an approximate inverse for the Schur complement as

$$\mathcal{S}^{-1} = (\mathcal{B} \mathcal{F}^{-1} \mathcal{B}^\top)^{-1} \quad (5.7)$$

$$\approx (\mathcal{B} \mathcal{B}^\top \tilde{\mathcal{F}}^{-1})^{-1} \quad (5.8)$$

$$\tilde{\mathcal{S}}^{-1} = \tilde{\mathcal{F}} (\mathcal{B} \mathcal{B}^\top)^{-1}. \quad (5.9)$$

Now the only task remaining is to find the approximate commutator of \mathcal{F} and we can use least squares minimization for that. Solving for the normal equations corresponding to (5.5) gives [11]

$$\tilde{\mathcal{F}} = (\mathcal{B} \mathcal{B}^\top)^{-1} \mathcal{B} \mathcal{F} \mathcal{B}^\top. \quad (5.10)$$

Substituting the above equation in the approximate inverse for the Schur complement (5.9) we get

$$\tilde{\mathcal{S}}^{-1} = (\mathcal{B} \mathcal{B}^\top)^{-1} \mathcal{B} \mathcal{F} \mathcal{B}^\top (\mathcal{B} \mathcal{B}^\top)^{-1}. \quad (5.11)$$

This is called BFBT approximation (because of the middle term sandwiched between two inverses) of the inverse Schur complement in the literature [11–13, 32] and has been successfully used in the context of Stokes and incompressible Navier–Stokes equations discretized with finite volume, finite difference and mixed FEM methods. In those cases, $\mathcal{B} \mathcal{B}^\top$ corresponds to the Poisson operator and instead of taking inverses one typically use a geometric multigrid or AMG cycle [11–13]. Also, for approximating \mathcal{F}^{-1} , AMG or geometric multigrid cycles are used [11–13]. Thus these choices provide a cheap approximation to the ideal preconditioner in equation (5.3) for a certain class of problems and discretizations. Scaled versions of the BFBT approximation are proposed in [11, 13, 23, 32] in order to improve the robustness in certain cases.

The HDG linear system for skeletal unknowns in equation (4.8) which comes after static condensation of volume unknowns is mostly algebraic in nature. Thus it is more difficult to analyze than stabilized or mixed FEM linear systems especially for complex systems like MHD. Moreover, our grouping of unknowns in equation (5.1) to arrive at the saddle point form is also algebraic and we can see that already in the \mathcal{F} matrix which contains part of the fluid block (without pressure) and the magnetic block. We base our choices for $(\mathcal{B} \mathcal{B}^\top)^{-1}$ and \mathcal{F}^{-1} considering this aspect.

In the context of HDG discretization of the incompressible MHD system, $\mathcal{B} \mathcal{B}^\top$ corresponds to a matrix of size $N_T \times N_T$ which is much smaller in size compared to \mathcal{F} . It is independent of the solution order p and the bandwidth is also small since it corresponds to the edge-average pressure which is piecewise constant per element. Since in high order HDG we try to minimize the number of elements while increasing the order to increase the computation to communication ratio the $\mathcal{B} \mathcal{B}^\top$ matrix is

small in this scenario. Thus as a first step we will use a parallel sparse direct solver `SuperLU_DIST` [21] for taking inverse of this matrix in the BFBT approximation. In our future work we will replace this part with preconditioned conjugate gradient solver of lenient tolerance to improve scalability. Some of the initial studies conducted in this direction shows promise.

For approximating \mathcal{F}^{-1} , we use one v-cycle of a system projection AMG solver from the ML library [14] of Trilinos project [17]. Similar to [36], we order the unknowns in the nodal block such that the degrees-of-freedom within each node appear consecutively. This helps to preserve the coupling between different variables during coarsening. The ordering of unknowns within each node is $(\hat{U}, \hat{B}^t, \hat{R})$ i.e., velocity trace unknowns are ordered first, followed by the tangent magnetic field and then the Lagrange multiplier. Other orderings are also possible and it can affect the performance of the AMG cycle. Since it is beyond the current scope of this article we intend to compare them in our future work. We use non-smoothed and uncoupled aggregation with a sparse direct solver on the coarsest level as in [36]. More details about the aggregation strategy employed in AMG can be found in [36]. The choice of smoothers inside the AMG cycle is critical and the mixed parabolic-hyperbolic nature of MHD together with the algebraic nature of the HDG trace system requires us to use strong smoothers such as ILU(0) and GMRES instead of standard smoothers like Jacobi and Gauss-Seidel.

Another choice for \mathcal{F}^{-1} is the multilevel preconditioner introduced in [26]. Since the coarse solver in the multilevel preconditioner is obtained by an approximation of the nested dissection direct solver it can also provide an effective approximation to \mathcal{F}^{-1} . We compare the results of the multilevel preconditioner to that of AMG for the approximation to \mathcal{F}^{-1} in section 6.4. In our numerical studies we observed that the performance of the scaled BFBT approximation is very similar to the non-scaled one (5.11) and hence we use that in all our experiments. In summary we use a right preconditioner

$$\begin{bmatrix} \tilde{\mathcal{F}}^{-1} & \tilde{\mathcal{F}}^{-1} \mathcal{B}^\top \tilde{\mathcal{S}}^{-1} \\ 0 & \tilde{\mathcal{S}}^{-1} \end{bmatrix}, \quad (5.12)$$

where $\tilde{\mathcal{F}}^{-1}$ is one v-cycle of AMG or the multilevel algorithm (Algorithm 1) in [26] and the approximate Schur complement inverse $\tilde{\mathcal{S}}^{-1}$ is given by the BFBT approximation (5.11). The $(\mathcal{B}\mathcal{B}^\top)^{-1}$ in the BFBT approximation is obtained by a linear system solve with parallel direct solver `SuperLU_DIST`.

6. Numerical results. In this section we test the performance of the block preconditioner on some of the transient test cases in incompressible resistive MHD considered before [9, 28, 36]. In particular, we consider 2D and 3D versions of the island coalescence problem, hydromagnetic Kelvin-Helmholtz (HMKH) instability and hydromagnetic lid-driven cavity problems. We use quadrilateral elements in 2D and hexahedral elements in 3D. For time integration we use the backward Euler time stepping for all the 3D test cases and five stage fourth order diagonally implicit Runge-Kutta (DIRK) method of [19] for all the 2D test cases. For the nonlinear solver we employ the Picard iteration scheme with a stopping criterion based on the discrete norm of the solution update vector given in [36]

$$\sqrt{\frac{1}{N_u} \sum_{i=1}^{N_u} \left[\frac{|\Delta \chi_i|}{\varepsilon_r |\chi_i| + \varepsilon_a} \right]^2} < 1.$$

Here, χ_i is any variable, $\Delta\chi_i$ is its corresponding update in the Picard iteration, N_u is the total number of unknowns and ε_a and ε_r are the absolute and relative tolerances which are set as 10^{-6} and 10^{-4} respectively. For the stopping tolerance of the linear solver, apart from the HMKH test case, we set the value to be 10^{-6} multiplied by the norm of the right hand side of the Picard linear system. For the HMKH test case, it turns out we need a stricter tolerance of 10^{-9} (not scaled by the norm of the right hand side) to make the Picard iterations converge.

For all the parallel results, we implemented our algorithms on top of the deal.II FEM library [1, 2]. The weak scaling studies are conducted in the Knights Landing (KNL) nodes of the Stampede2 supercomputer at the Texas Advanced Computing Center. Each node of KNL consists of 68 intel Xeon Phi 7250 1.4GHz processors with 4 threads per core. It has 96GB DDR4 RAM along with 16GB high speed MCDRAM which acts as L3 cache. We have used only MPI parallelism even though our deal.II code has task based parallelism using thread building blocks (TBB) in addition to MPI. The reasons for this choice are: (i) to have memory locality and avoid memory contention which may complicate the weak scaling studies (ii) the main focus of this study, which is the linear solver part, uses ML from Trilinos which does not have the threads support. In our future work we will use the second generation Trilinos library MueLu [30] instead of ML as it provides support for threads and GPU.

6.1. Island coalescence. Magnetic reconnection is a fundamental phenomenon by which a magnetic field changes its structure and is accompanied by conversion of magnetic field energy into plasma energy and transport [36]. Many physical phenomena which occurs in outer space such as solar flares, coronal mass ejections involve magnetic reconnection as an important driving mechanism. It is also important in a laboratory scenario, especially in fusion experiments to understand and control plasma disruptions which can lead to loss in plasma confinement and also damages to the machine. Since fusion reactors like tokamak are typically designed to handle only certain maximum number of these disruptions, understanding and controlling these phenomena is of significant interest to the fusion and in general plasma community. More details about magnetic reconnection can be found in [5, 15, 16].

While magnetic reconnection is important for its physical significance, it is also characterized by disparate spatial and temporal scales which serves as an ideal test bed for testing the robustness of our preconditioners/solvers. In this section we consider a specific reconnection problem which is the island coalescence studied in [6, 36]. It initially consists of two islands embedded in a Harris current sheet as shown in Figure 6.1(a). A perturbation to the initial configuration and the combined magnetic field causes the center of the islands (referred as the o-points) to move towards each other and eventually coalesce to form one island. When the reconnection happens, the islands form a ‘x’ structure in the center of the domain as shown in Figures 6.1(d) and 6.4. In what follows we will briefly describe the settings of this problem and then evaluate the performance of our preconditioner in this case.

The domain is $[-1, 1]^d$, where d is the dimension. The boundary conditions are periodic in the x-direction on the left and right faces and also in the z-direction on the back and front faces. On the top and bottom faces in the y-direction, for the magnetic part, perfect conducting boundary conditions described by zero normal magnetic field $\mathbf{b} \cdot \mathbf{n} = 0$ and zero tangential electric field $\mathbf{n} \times \mathbf{E} = 0$ are applied. For the fluid part on the top and bottom faces, mirror boundary conditions described by zero normal velocity $\mathbf{u} \cdot \mathbf{n} = 0$ and zero shear stress are applied. The Lagrange multiplier r is set as zero on all the boundaries. We refer the readers to [37] for an application of these

boundary conditions in the context of HDG discretizations.

The initial conditions consists of zero fluid velocity ($\mathbf{u}^0 = \mathbf{0}$), and the magnetic field given by

$$\mathbf{b}^0 = \left(\frac{\sinh(2\pi y)}{\cosh(2\pi y) + \epsilon \cos(2\pi x)}, \frac{\epsilon \sin(2\pi x)}{\cosh(2\pi y) + \epsilon \cos(2\pi x)}, 0 \right),$$

where in 2D the first two components of the field values are used. Here, ϵ refers to the width of the island and we choose it to be 0.2 as in [36]. In order for the initial configuration to be in equilibrium a forcing of $\mathbf{g} = \nabla \times \mathbf{J}^0$ is used where

$$\mathbf{J}^0 := \mathbf{J}(t=0) = \left(0, 0, -\frac{2\pi\kappa(1-\epsilon^2)}{\text{Rm}(\cosh(2\pi y) + \epsilon \cos(2\pi x))^2} \right).$$

For the momentum equation zero forcing ($\mathbf{f} = \mathbf{0}$) is selected. To set the islands into motion in a reproducible manner rather than relying on the accumulation of round-off error an initial perturbation of

$$\delta\mathbf{b}^0 = \sigma \left(\frac{\pi}{2} \cos(\pi x) \sin\left(\frac{\pi y}{2}\right) \cos(\pi z), -\pi \sin(\pi x) \cos\left(\frac{\pi y}{2}\right) \cos(\pi z), 0 \right),$$

is used with the value of $\sigma = 10^{-3}$ which sets the magnitude of perturbation [37]. For 2D, the first two components are used without the z -term. As described in [37] we choose the characteristic velocity as Alfvén speed which gives $\kappa = 1$. Also in all our numerical experiments we set the fluid Reynolds number and magnetic Reynolds number (which is Lundquist number in this case) equal to each other.

Let us choose a Lundquist number $S = 10^3$, and a $16 \times 12 \times 14$ clustered mesh of order $p = 5$. Figure 6.1, shows the evolution of the z -component of current by taking a slice of the contour plot at mid-plane $z = 0$. As can be seen the perturbation in the z -direction causes the current contours to bend and results in a highly kinked state as evidenced in Figure 6.1(d). Our results show good agreement (visually) with the results in [6, 36].

Now we compare the performance of three preconditioners for this problem in a weak scaling sense i.e., we increase the problem size proportionally with the increase in number of processors so that the number of elements per processor remains constant. We take 4^3 , 8^3 , 16^3 and 32^3 elements and 2, 16, 128 and 1024 processors respectively so that we have 32 elements per core. A time stepsize of 0.1 is selected and all the results are averaged over six time steps. The nonlinear Picard solver takes on average 3.2 – 4 iterations in all the cases.

First of the preconditioners is a one level domain decomposition method with an incomplete factorization sub-domain solver with zero fill-in (ILU(0)) and overlap of one¹ (denoted as DD, ILU(0) in Figure 6.2 and let us refer to this as DD with ILU(0)). The other two preconditioners are the block preconditioners given in equation (5.12) with BFBT approximation for \tilde{S}^{-1} and one AMG v-cycle for \tilde{F}^{-1} . The difference between them is the smoothing inside AMG, in one of them we use the ILU(0) smoother of overlap one (denoted as BFBT+AMG, ILU(0) in Figure 6.2 and let us refer to this as BFBT+AMG with ILU(0)), whereas in the other one we use the GMRES preconditioned by ILU(0) of overlap zero² as smoother (denoted as BFBT+AMG, GMRES

¹Here, overlap one means each processor will include its own set of rows and in addition it also includes the rows corresponding to its non-zero columns.

²Here, overlap zero means each processor will include only its own set of rows and thus no communication is needed.

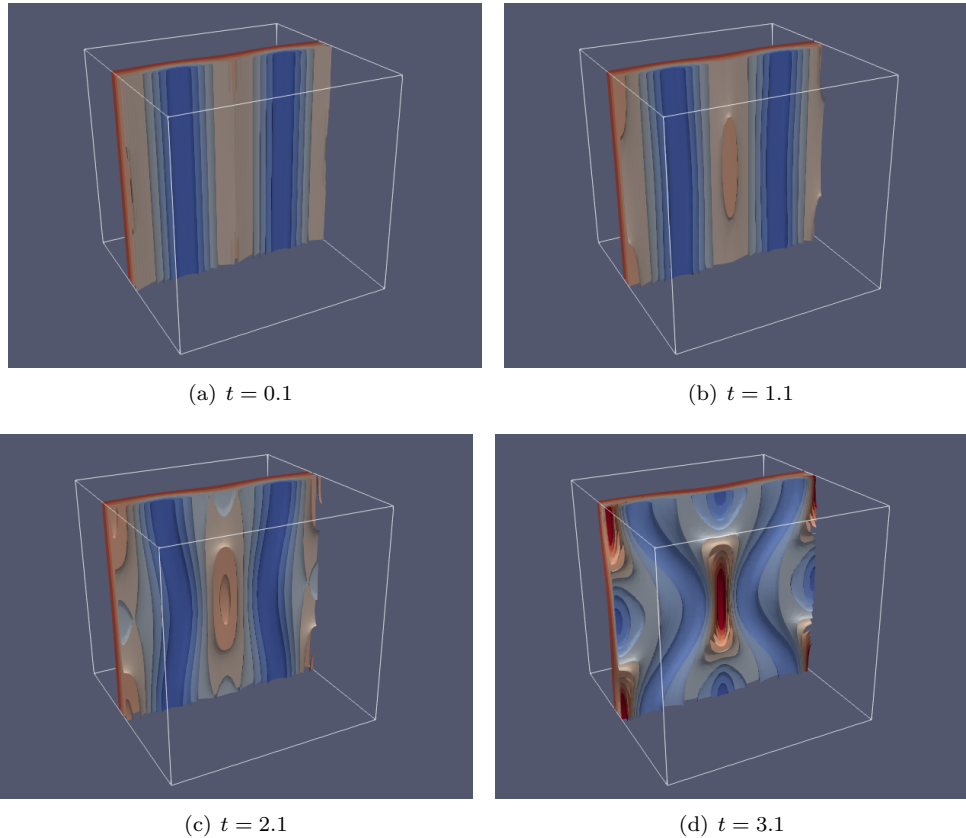


Fig. 6.1: Evolution of the z -component of the current (J_z) with time. The contours of J_z show a highly kinked state at $t = 3.1$ due to the perturbation in the z -direction.

in Figure 6.2 and let us refer to this as BFBT+AMG with GMRES). The reason for these non-standard choice of smoothers is, classical smoothers like Jacobi, Chebyshev and Gauss–Seidel did not result in converging iterations. This is also observed in [22] for linear systems arising from stabilized FEM discretization of MHD. Thus it indicates that strong smoothers are needed for AMG cycles applied to linear systems coming from incompressible resistive MHD.

We perform three pre- and three post-smoothing steps (in the case of GMRES smoother, these denote the number of inner iterations), whereas in the DD with ILU(0) preconditioner we perform three smoothing steps. The outer iterations are performed with GMRES for the DD with ILU(0) and the BFBT+AMG with ILU(0) preconditioners. For the BFBT+AMG with GMRES, we use flexible GMRES (FGMRES) [33] for the outer iterations due to the nonlinear nature of the inner iterations. In both cases similar to [36] we use non-restarted versions as it may result in degradation of convergence.

We compare the performance in terms of average iterations per Picard step and average time per Picard step in Figure 6.2. From Figure 6.2(a) for solution order $p = 4$, we can see that the iterations of DD with ILU(0) preconditioner increases much faster

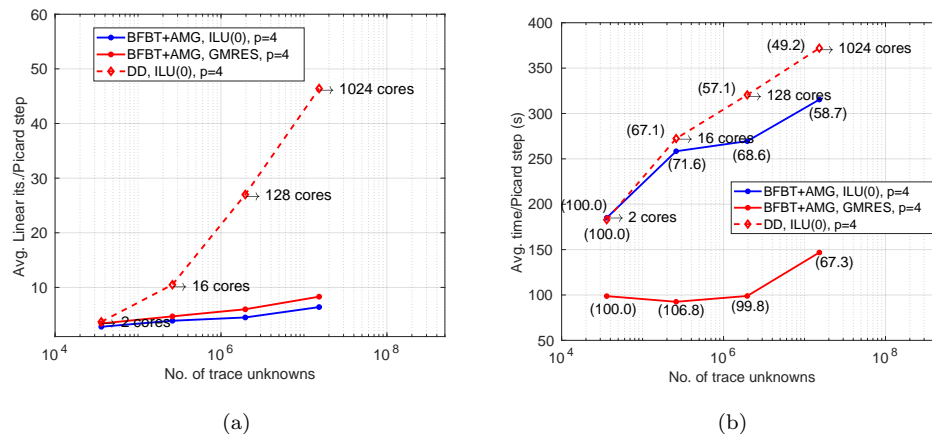


Fig. 6.2: 3D island coalescence problem: weak scaling study of average iterations per Picard step (left) and average time per Picard step (right) for three preconditioners and solution order $p = 4$. The markers in BFBT+AMG with ILU(0) and GMRES also represent the same number of processors as in DD with ILU(0). The values within parentheses in the right figure represent weak scaling parallel efficiencies.

than the other two block preconditioners and this is due to the lack of coarse solvers. Similar results are also observed in [36] for the stabilized FEM discretization. The average linear iterations per Picard step for the two block preconditioners are less than the one level domain decomposition preconditioner and the growth with number of unknowns/processors (here the number of unknowns refers to the number of trace unknowns only) is also very mild. Between ILU(0) and GMRES smoothers we can see that the GMRES smoother takes slightly more iterations than the ILU(0).

In Figure 6.2(b), we compare the average time per Picard step for the three preconditioners and again DD with ILU(0) preconditioner takes more time compared to the block preconditioners. However, a fact to notice is that the large difference in iteration counts evidenced in Figure 6.2(a) between DD with ILU(0) and BFBT+AMG with ILU(0) is not much reflected in the timing figure in 6.2(b). This is because ILU(0) with overlap one spends most of the time in the setup cost and very little time in the application of the preconditioners. Since the setup cost in both DD with ILU(0) and BFBT+AMG with ILU(0) are very similar the difference comes only from the application of the preconditioners which is high for DD with ILU(0) due to larger number of iterations. The scenario for the GMRES smoother is exactly opposite with very little time spent for the setup and most of the cost coming from the application or solving part of the preconditioner. This reflects in the timing results in Figure 6.2(b) with BFBT+AMG with GMRES smoother taking the least time (in spite of its iteration count bit higher than ILU(0) smoother) and more than two times faster than the other two preconditioners. We want to make a remark here that even though the number of volume unknowns per core is same in this weak scaling study the number of trace unknowns per core is not exactly the same and the cases of 16 cores, 128 cores and 1024 cores has slightly less number of trace unknowns per core compared to the 2 core case. This is the reason in Figure 6.2(b) the time per Picard step for GMRES smoother decreases slightly for 16 cores case even though the iterations increase a bit

compared to that for 2 cores. However, asymptotically this difference gets negligible and hence does not affect much our inferences.

S	DD, ILU(0)		BFBT+AMG, ILU(0)		BFBT+AMG, GMRES	
	iterations	time (s)	iterations	time (s)	iterations	time (s)
10^3	94	489.4	3.5	287.8	5.3	124.4
10^4	*	*	*	*	6	127.6
10^5	*	*	*	*	7.5	128.2
10^6	*	*	*	*	7.6	131.2

Table 6.1: 3D island coalescence problem. Robustness study with respect to Lundquist number S : iterations and time represent the average number of iterations taken per Picard step and the average time per Picard step. “*” indicates the preconditioners did not reach the specified tolerance for the maximum number of iterations which is taken as 1000 for DD with ILU(0) and 200 for BFBT+AMG with ILU(0). The time step in this study is $\Delta t = 0.05$ and the mesh, solution order and number of cores are 32^3 , $p = 4$ and 1024 respectively. The average number of Picard iterations taken is approximately 3.

In Table 6.1 we compare the robustness of the preconditioners with respect to Lundquist number S . Clearly, BFBT+AMG with GMRES is more robust than the other two preconditioners and takes nearly constant number of iterations and time per Picard step for the parameters mentioned in Table 6.1.

Now, in addition to computational time and robustness another important aspect to take into account is, ILU(0) smoothers with overlap one require lot of memory and this is much pronounced at high solution orders. In our numerical experiments we found that for solution orders greater than four, in the KNL nodes of Stampede2, we are able to use only 8 cores per node or less even though the system has 68 cores per node due to memory limitations. The GMRES smoother (GMRES preconditioned by ILU(0) with overlap zero) on the other hand has less memory requirements than the ILU(0) smoother with overlap one and this is the reason we test only BFBT+AMG with GMRES smoother for solution orders $p = 5, 6$ in Figure 6.3.

In Figure 6.3, the average number of iterations and time per Picard step are shown for the BFBT+AMG with GMRES smoother for solution orders $p = 5, 6$. The iteration counts are very similar to those observed for $p = 4$ in Figure 6.2(a) with a mild increase with respect to mesh refinements. The time per Picard step however, for $p = 4, 5$ with 1024 cores and $p = 6$ with 2048 cores show a significant increase compared to 128 and 256 cores respectively. This is a result of two things, (i) increase in iteration count; (ii) coarsening in AMG. We have not done repartitioning with the uncoupled aggregation performed in AMG and at high processor counts this resulted in fewer levels (3 or 4) in the AMG hierarchy with larger problem sizes on the coarsest level. Since, we use a serial sparse direct solver on the coarsest level the timing increased. This trend is observed in the other two numerical experiments also and especially in Figure 6.11 for the lid driven cavity problem. In that case we have almost constant iteration counts which is reflected in the timing till 256 processors and after that both in 1024 and 2048 processors we see some increase in timing. In our ongoing work we are experimenting with different coarsening strategies in AMG and the initial studies have shown promise. We will report these findings as well as optimization of the other components used in the block preconditioning strategy in

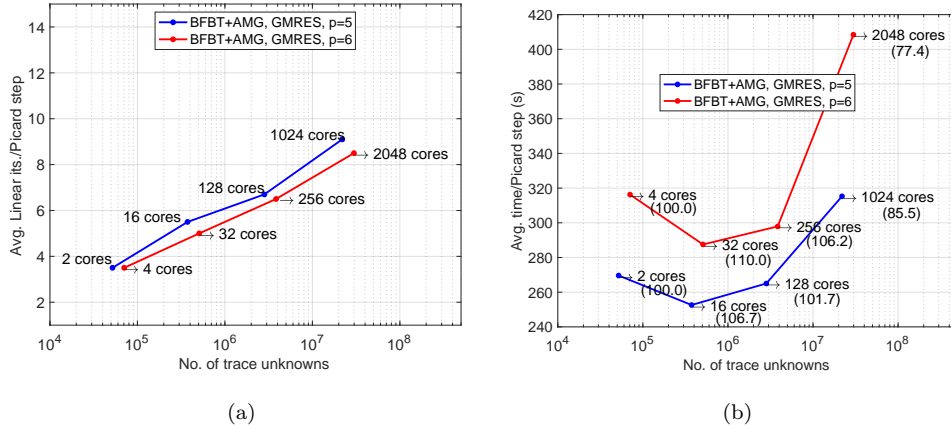


Fig. 6.3: 3D island coalescence problem. BFBT+AMG with GMRES smoother: weak scaling study of average iterations per Picard step (left) and average time per Picard step (right) for solution orders $p = 5, 6$. The values within parentheses in the right figure represent weak scaling parallel efficiencies.

the future.

$N_T = 32,768$, $N_{trace} = 15.2M$, $p=4$, $\Delta t = 0.1$, averaged over 6 time steps				
#cores	time/Picard [s]	N_T /core	Trace DOF/core	efficiency [%]
128	211.6	256	118.4K	-
256	126.8	128	59.2K	83.4
512	64.2	64	29.6K	82.4
1024	36.3	32	14.8K	73
2048	19.4	16	7.4K	68
4096	16.6	8	3.7K	40
6144	14.9	5.3	2.5K	29.6

Table 6.2: 3D island coalescence problem. Strong scaling study for BFBT+AMG with GMRES smoother for solution order $p = 4$. The simulation is carried out in the Skylake nodes of Stampede2 supercomputer.

In Tables 6.2 and 6.3 we study the strong scalability of BFBT+AMG with GMRES smoother for solution orders $p = 4, 6$. We see a good strong scaling performance and the efficiency improves with increase in order for similar number of trace unknowns/core due to increased computation to communication ratio. For the strong scaling study we used the Skylake nodes of Stampede2 supercomputer and since it has a higher clock speed (2.1GHz) compared to the KNL nodes (1.4GHz) the average time per Picard step is 4 – 5 times lesser than that for KNL nodes. Of the three preconditioners since the BFBT+AMG with GMRES smoother is faster, more robust and requires less memory we will consider only that in the subsequent numerical studies. Also, since the strong scaling performance is not very much problem dependent we only study the performance in terms of weak scaling.

$N_T = 32,768$, $N_{trace} = 29.8M$, $p=6$, $\Delta t = 0.1$, averaged over 6 time steps				
#cores	time/Picard [s]	N_T /core	Trace DOF/core	efficiency [%]
512	290	64	58.4K	-
1024	129.5	32	29.2K	112
2048	82.6	16	14.6K	87.7
4096	46.6	8	7.3K	77.7
8192	39.4	4	3.7K	46

Table 6.3: 3D island coalescence problem. Strong scaling study for BFBT+AMG with GMRES smoother for solution order $p = 6$. The simulation is carried out in the Skylake nodes of Stampede2 supercomputer.

We now use the BFBT+AMG with GMRES preconditioner to simulate a challenging problem which is 2D island coalescence at high Lundquist numbers. Here as an example we consider a Lundquist number of $S = 10^7$. The significance of this problem is that at high Lundquist numbers the thin current sheet which forms at the center of the domain during reconnection breaks and gives rise to small structures called plasmoids [4, 18]. The dynamics of this problem is very different from the low Lundquist number cases where the islands monotonically approach each other and coalesce to a single island.

The settings of this experiment are as follows: While for the scaling studies we used a fixed time stepsize of $\Delta t = 0.1$, in this case we use an adaptive time step where we initially start with a stepsize of 0.05 and if the Picard iteration fails to converge in 20 iterations we cut the stepsize by half and try again. This is essential for capturing the highly nonlinear evolution of this problem and we observed a stepsize of 0.0015625 during the plasmoid formation and evolution stages. Once the time stepsize is cut by half we do not increase it later in the simulation, while increasing the stepsize may help in reducing the overall time of the simulation our focus here is to simulate the correct physics and also test the robustness of our preconditioner. The domain is discretized by 128×128 uniform elements and solution order $p = 9$. For time stepping we use the five stage fourth order DIRK scheme. The problem is run on 512 cores in the Skylake nodes of Stampede2 supercomputer.

Figure 6.4 shows the formation of x-structure in the center of the domain at $t = 5.2$ similar to the 3D problem in Figure 6.1(d). We zoom in to the box marked at the center of the domain in Figure 6.4 to see clearly the formation and evolution of plasmoids. Figure 6.5 shows the current and pressure corresponding to the box region marked in Figure 6.4 at different times. From these two figures we can clearly see bubble like structures which are called plasmoids emanating from the breakdown of the thin current sheet and moving in the vertical direction. At least from Figure 6.5 we can see two prominent plasmoids one moving downwards and the other upwards. However, there are lot more tiny plasmoids which continuously appear and merge as time proceeds. This problem clearly shows the multiscale nature of the magnetic reconnection phenomenon in both space and time. The island widths are of $\mathcal{O}(0.1)$, whereas the size of plasmoids are of $\mathcal{O}(0.01)$. Similarly the time scale in which the island moves is almost an order of magnitude larger than the plasmoid time scales. The linear solver iterations for this problem is mostly less than 10 for majority of the Picard steps with some exceptions taking between 15 – 20. Thus the BFBT+AMG preconditioner with GMRES smoother seems to be fairly robust for this challenging

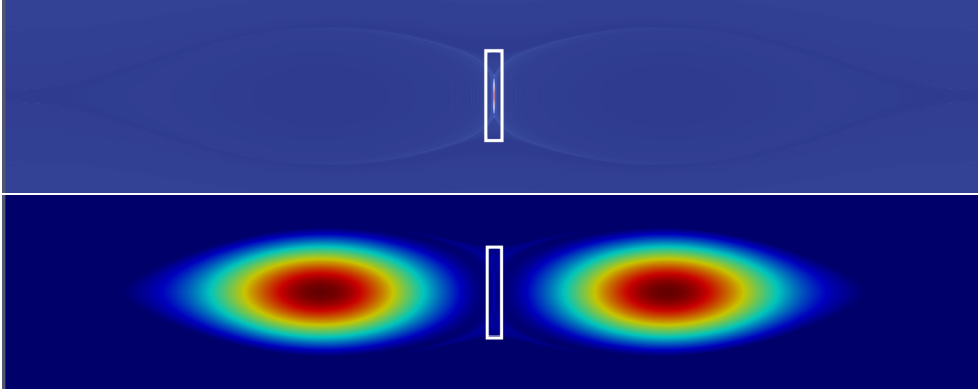


Fig. 6.4: 2D island coalescence problem: Current (top) and pressure (bottom) at time $t = 5.2$ showing the coalescence of the islands. In Figure 6.5 we will focus on the box region marked in the central portion of the above figures.

problem which involves multiscale physics in space and time. The current plots in Figure 6.5 show some grid scale structures necessitating more elements in those areas or application of filters/artificial viscosity. We will investigate more into slope limiting, filtering and artificial viscosity strategies for our high-order scheme in the future works.

6.2. Hydromagnetic Kelvin-Helmholtz instability. In this section we consider the 2D and 3D versions of hydromagnetic Kelvin-Helmholtz (HMKH) instability problem studied in [9, 28, 36]. This problem also involves magnetic reconnection similar to the island coalescence problem in the previous section. The domain we consider is $[0, 4] \times [-2, 2]$ in 2D and $[0, 4] \times [-2, 2] \times [0, 2]$ in 3D. The initial conditions consists of two counter flowing conducting fluids of constant velocities given by $\mathbf{u}^0(x, y \geq 0, z) = (1, 0, 0)$ and $\mathbf{u}^0(x, y < 0, z) = (-1, 0, 0)$ and a Harris sheet magnetic field defined by $\mathbf{b}^0(x, y, z) = (B_0 \tanh(y/\delta), 0, 0)$. We choose a zero forcing for both fluid and magnetic equations. Similar to the island coalescence problem, the boundary conditions are periodic in x- and z-directions. On the top and bottom faces the fluid boundary conditions are same as the island coalescence problem with zero normal velocity and zero shear stress and the magnetic field is defined by the Harris sheet in the initial condition. The Lagrange multiplier r is set as zero on all the boundaries. We select the following parameters as per [36]: $\kappa = 1$, $\text{Re} = \text{Rm} = 10^4$, $B_0 = 0.3333$ and $\delta = 0.1$. These values along with $\rho = \mu_0 = 1$ gives a super Alfvénic Mach number of $M_A = u/u_A = 3$ as described in [36]. If $M_A > 1$ then the magnetic field is not strong enough to suppress the instabilities and the shear layer is Kelvin-Helmholtz unstable. Thus the initial disturbances eventually grow to form vortices which roll up and merge as time proceeds.

First, we consider the 2D HMKH problem discretized in a 128×128 mesh with solution order $p = 6$. We use a time stepsize of $\Delta t = 0.001$ in the five stage fourth order DIRK method. As mentioned in the beginning of the numerical section we needed a stricter tolerance of 10^{-9} in the linear solver to make the Picard iterations converge for this problem up to a relative tolerance of 10^{-4} . The preconditioner is BFBT+AMG with GMRES smoother and the outer iterations are carried out by FGMRES. In Figure 6.6, the evolution of vorticity with time is shown along with

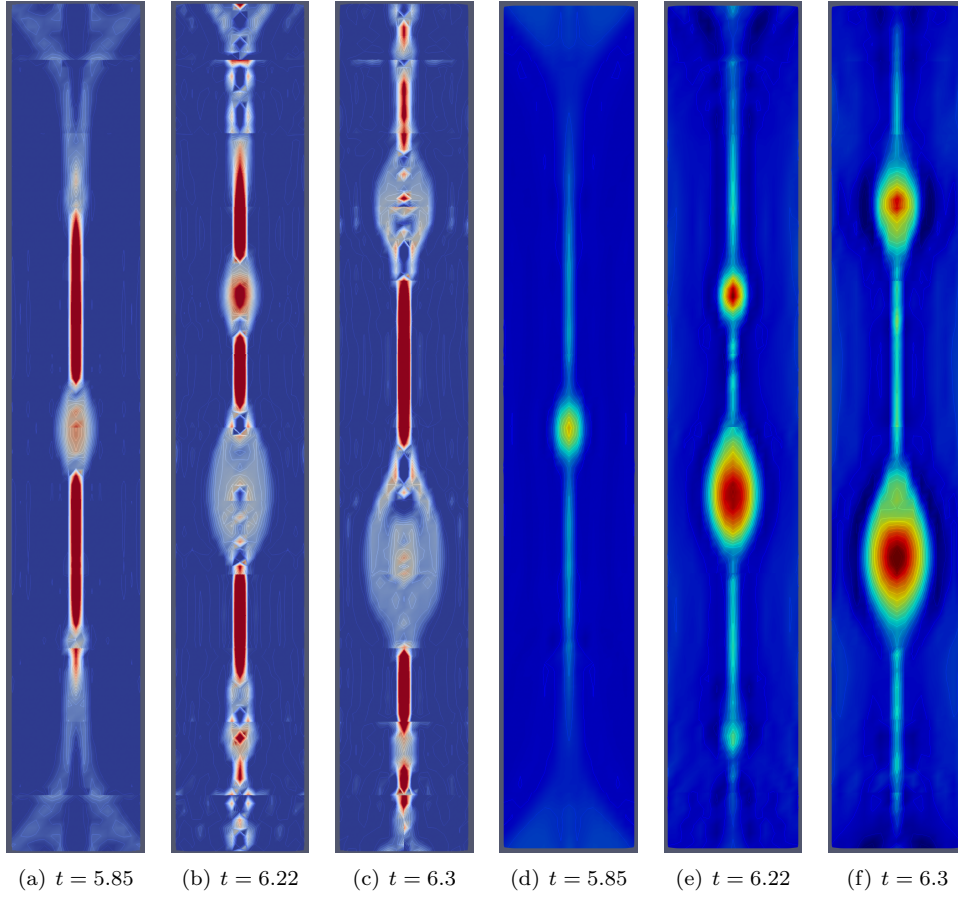


Fig. 6.5: 2D island coalescence problem: Current (first three from left to right) and pressure (last three) plots at the indicated times showing the formation and evolution of plasmoids with time.

the magnetic vectors marked by arrows. The figure shows the roll up of vortices to form the familiar cat-eye pattern and the magnetic vectors bends and follows the fluid evolution as time proceeds. In Figure 6.7, we show the 3D HMKH problem discretized in a $20 \times 24 \times 7$ mesh clustered around the region of solution and solution order $p = 5$. An initial time stepsize of $\Delta t = 0.025$ is selected for the backward Euler time stepping and the adaptive time stepping procedure described in the previous section is employed. Here also as in 2D we see the rollup of vortices and the magnetic vectors following them.

Next, we study the weak scaling performance of the BFBT+AMG with GMRES smoother for the 3D HMKH problem. For this we used a fixed time stepsize of $\Delta t = 0.01$ in the backward Euler time stepping and the results are averaged over six time steps. We used $8 \times 8 \times 10$, $16 \times 16 \times 10$, $32 \times 32 \times 10$ and $64 \times 64 \times 10$ meshes corresponding to 32, 128, 512 and 2048 processors respectively. Thus the number of elements per processor in this case is 20. The CFL ($p^2 \Delta t / h_{min}$) ranges

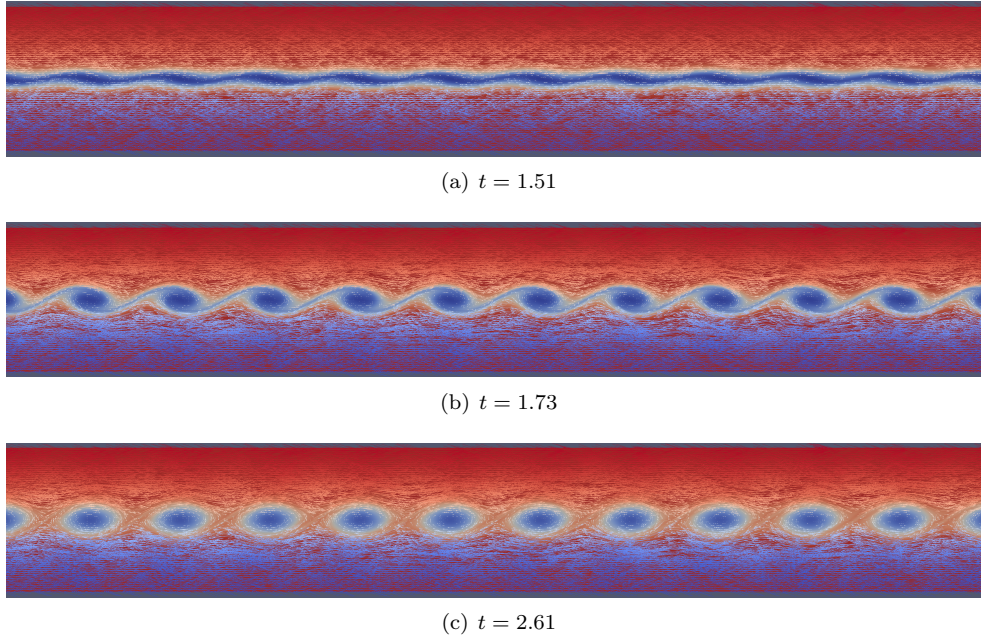


Fig. 6.6: 2D HMKH problem: Vorticity plots at the indicated times along with the magnetic vectors (marked as arrows). The magnetic vectors are scaled by their magnitude and are colored by the x-component of the magnetic field (b_x). The red arrows on the top represent the positive values of b_x and blue arrows on the bottom represent the negative values.

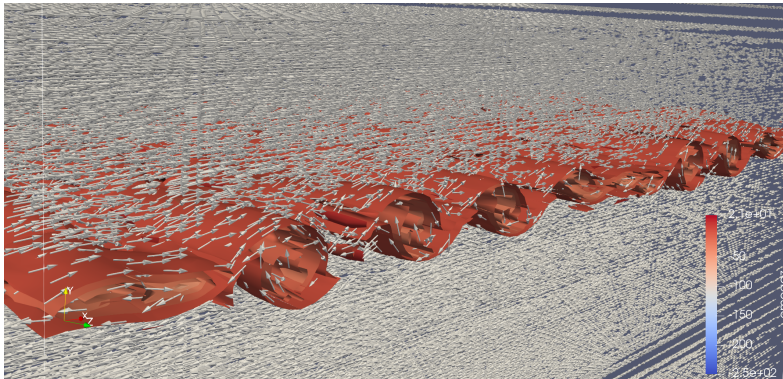


Fig. 6.7: 3D HMKH problem: Z -component of vorticity contours along with magnetic vectors at time $t = 2.0625$. The magnetic vectors are not colored and scaled in this figure to improve visibility.

from 0.8 to 2.56 for solution order $p = 4$ and 1.25 to 4 for $p = 5$ corresponding to the mesh sizes and time stepsize. The Picard solver took approximately 2 iterations in all the cases. Figure 6.8 shows the average iteration counts and time per Picard

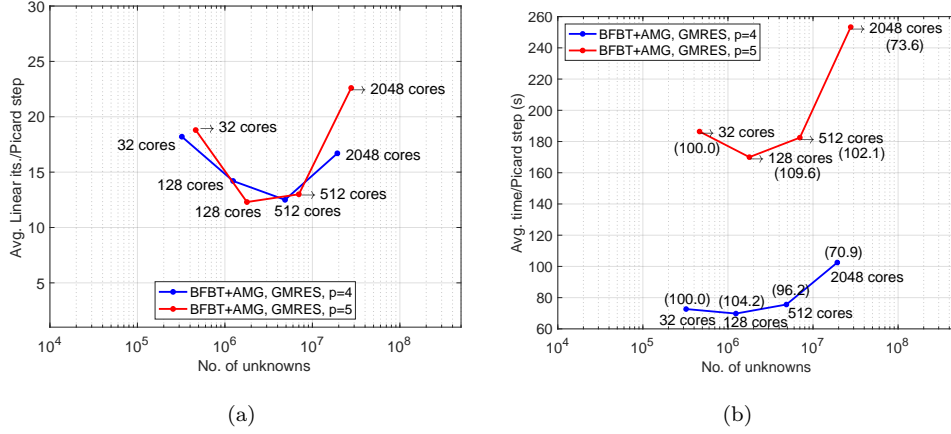


Fig. 6.8: 3D HMKH problem. BFBT+AMG with GMRES smoother: weak scaling study of average iterations per Picard step (left) and average time per Picard step (right) for solution orders $p = 4, 5$. The values within parentheses in the right figure represent weak scaling parallel efficiencies.

step, since the tolerance of the iterative solver in this case (10^{-9}) is stricter than for the island coalescence problem (10^{-6}) we see an increase in overall iteration counts. However, the number of iterations still lies mostly between 10 – 20 which is moderate considering the tight tolerance of 10^{-9} and the maximum CFL numbers of 2.56 and 4 for $p = 4$ and 5 respectively. The average time per Picard step reflects the trend in the iteration count together with the decrease in scalability in the 2048 processors regime as discussed in the previous section on island coalescence.

6.3. Lid driven cavity. In this section we consider a hydromagnetic version of the classical lid driven cavity problem. The settings of this problem follow closely [28]. Even though we simulated the 2D version of this problem also, here we present the results only for the 3D problem for brevity. The domain is $[-0.5, 0.5]^3$, with no slip boundary conditions of $\mathbf{u} = \mathbf{0}$ applied on all the walls except the top one where we apply a velocity of $\mathbf{u} = (1, 0, 0)$ which drives the flow. For the magnetic field we set the tangential component on each wall as $\mathbf{b} \times \mathbf{n} = (-1, 0, 0) \times \mathbf{n}$ which acts from right to left. The Lagrange multiplier r is set as zero on all the boundaries. Both initial conditions and forcings are chosen as zero. We choose the following parameters: $\kappa = 1$, $\text{Re} = \text{Rm} = 1000$ which corresponds to a Hartmann number of $Ha = \sqrt{\kappa \text{ReRm}} = 1000$.

First, we consider a 8^3 uniform mesh, solution order $p = 6$ and an initial time stepsize of $\Delta t = 0.0125$ in the adaptive time stepping with backward Euler method. The linear and nonlinear solver tolerances and the stopping criteria are same as the ones used for the island coalescence problem. Figure 6.9 shows the evolution of the streamlines together with the velocity vectors in the $x = 0$, $y = 0$ and $z = 0$ planes. The presence of the third dimension allows the streamlines to curl in the z -direction in Figures 6.9(b) and 6.9(c) which gives rise to complex velocity patterns. In Figure 6.10 the corresponding magnetic field lines along with the magnetic vectors are shown. Because of the applied tangential magnetic field from right to left we can see the

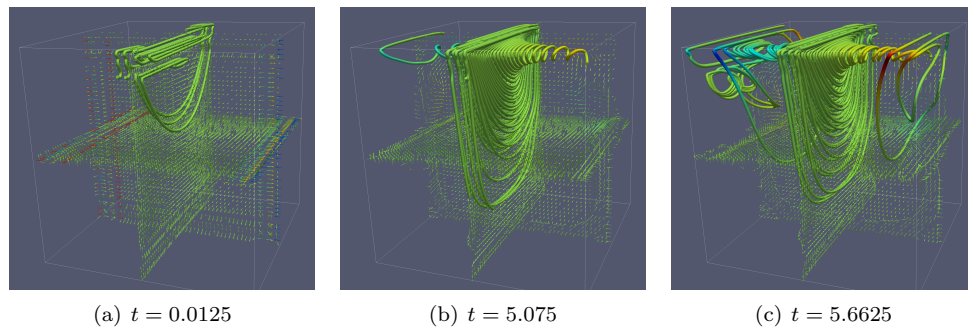


Fig. 6.9: 3D lid driven cavity problem: Evolution of the streamlines and velocity vectors with time. Both the streamlines and the velocity vectors are colored by the z -component of velocity and the velocity vectors are not scaled.

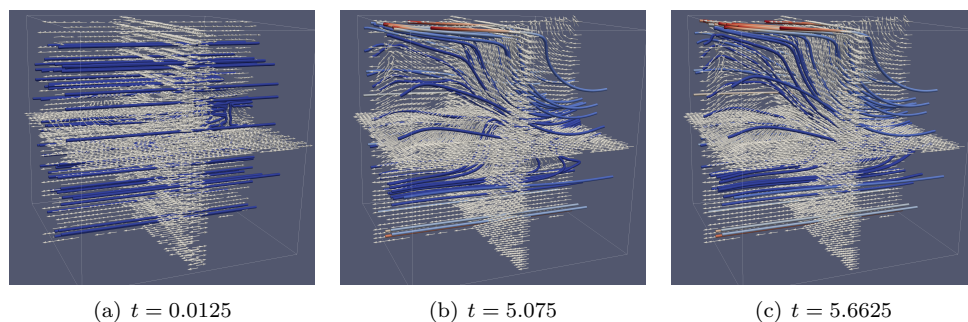


Fig. 6.10: 3D lid driven cavity problem: Evolution of the magnetic field lines and magnetic vectors with time. The magnetic vectors are not colored and scaled and the field lines are colored by b_x .

magnetic lines and the vectors going from right to left with some bending caused by the interaction with the fluid components.

For the weak scaling study we consider a fixed time stepsize of $\Delta t = 0.0025$ for solution orders $p = 4, 5$ whereas for $p = 6$ we consider $\Delta t = 0.001$ in the backward Euler method. The meshes we consider are 4^3 , 8^3 , 16^3 and 32^3 corresponding to 4, 32, 256 and 2048 processors respectively with 16 elements per core. The CFL in this case ranges from $0.16 - 1.28$ for $p = 4$, $0.25 - 2$ for $p = 5$ and $0.14 - 1.15$ for $p = 6$. The Picard iterations in all the cases range from $3.5 - 4.7$. We also tested with $\Delta t = 0.01$ for $p = 4$ and observed that the iterations of the linear solver remains more or less the same as that for $\Delta t = 0.0025$ whereas the average Picard iterations are 5.3, 6.5, 7.5 and 9.3 corresponding to the four mesh sizes. In Figure 6.11 we show the average iterations and time per Picard step for the BFBT+AMG preconditioner with GMRES smoother and the results are averaged over six time steps. Compared to the previous two experiments, in this case we have a fairly constant iteration count with mesh refinements for all the solution orders. In Figure 6.11(b) we again see some increase in time per Picard step for 2048 cores which in this case comes only from the

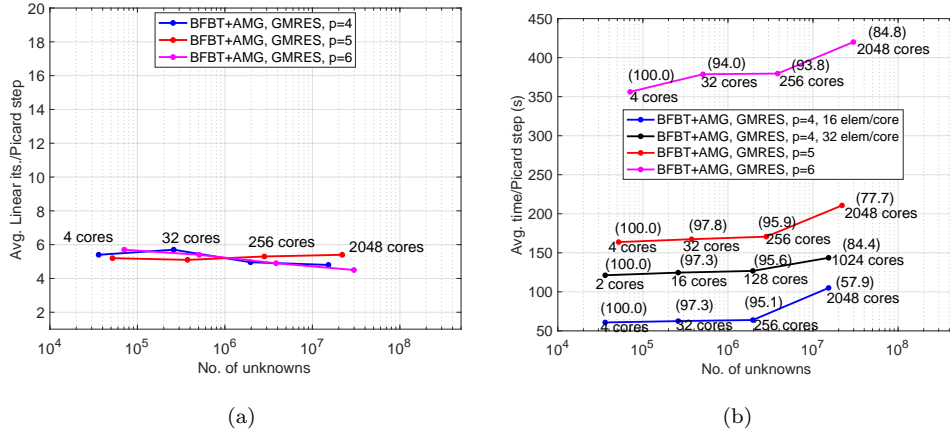


Fig. 6.11: 3D lid driven cavity problem. BFBT+AMG with GMRES smoother: weak scaling study of average iterations per Picard step (left) and average time per Picard step (right) for solution orders $p = 4, 5, 6$. The values within parentheses in the right figure represent weak scaling parallel efficiencies.

coarsening in AMG and other components of the block preconditioner as we have a flat iteration count. We consider one more case for solution order $p = 4$ with 2, 16, 128 and 1024 cores in Figure 6.11(b), and this shows better weak scaling performance than the other case with 2048 cores for the finest mesh size. This once again highlights the need for investigation of better coarsening strategies in the AMG preconditioner for better scalability at large number of cores.

6.4. BFBT+Multilevel preconditioner. The AMG preconditioner used for the approximation of \mathcal{F}^{-1} in the block preconditioner contributes to the dominant cost and in this section we will consider an alternative to it and compare the performance. To that extent we will apply the multilevel preconditioner introduced in [26] for $\tilde{\mathcal{F}}^{-1}$ in the block preconditioning (5.12). The problem we consider is the 2D island coalescence studied in section 6.1. We will also compare the performance of the iterative solver with respect to nested dissection direct solver in this section.

In [26] the multilevel preconditioner is introduced for problems with scalar trace unknowns and here we will extend the idea in a natural manner and apply it to vector valued trace unknowns. Similar to AMG, we order the unknowns such that on each edge all the trace unknowns (except edge average pressure) corresponding to the first node are ordered first, followed by the unknowns in the second node and so on. The ordering of unknowns within each nodal point is $(\hat{U}, \hat{B}^t, \hat{R})$.

We then apply one v-cycle of the iterative multilevel algorithm, Algorithm 1 in [26], for $\tilde{\mathcal{F}}^{-1}$. For the coarse-solver in the multilevel algorithm we use the enriched multilevel approach (EML) because of its robustness and better performance compared to the non-enriched version [26]. By means of several numerical experiments we observed that the number of smoothing steps in the block-Jacobi part of the multilevel algorithm, $m_1 = 0$ and $m_2 = 1$ i.e., only one post-smoothing, gives the least number of outer GMRES iterations and we use that in all the cases. We also observed that increasing the number of smoothing steps generally leads to more number of it-

erations in this case and post-smoothing performs better than pre-smoothing. Since the nodal block (\mathcal{F}) in the HDG discretization of MHD is a non-symmetric mixed parabolic-hyperbolic system and for the most part it is purely algebraic we cannot in general expect better performance by increasing the number of smoothing steps. The number of iterations also depends on how the fine scale solver (block-Jacobi) in the multilevel algorithm interacts with the coarse-scale solver (EML) by means of capturing the overall spectrum and we do not have a clear understanding of this yet. In our future work we will investigate this by means of Fourier analysis and it can guide us to select the appropriate number of smoothing steps as well as the choice of the fine scale solver.

Having described the specifications of the multilevel algorithm for $\tilde{\mathcal{F}}^{-1}$ we will now compare BFBT+multilevel preconditioner (referred as BFBT+EML) to BFBT+AMG with GMRES smoother. The outer iterations are carried out with GMRES in the case of BFBT+multilevel preconditioner and FGMRES for BFBT+AMG with GMRES smoother. For the time discretization we use the backward Euler time stepping with a fixed time stepsize of $\Delta t = 0.1$. The results are averaged over six time steps for all the cases except 128×128 and 256×256 meshes where we average over three time steps. We choose a Lundquist number of $S = 10^3$. We run the AMG solver serially in this case to compare with the serial implementation of the multilevel method. So this study is mainly to assess the algorithmic scalability of multilevel and AMG preconditioners with respect to mesh refinement, solution order and Lundquist number.

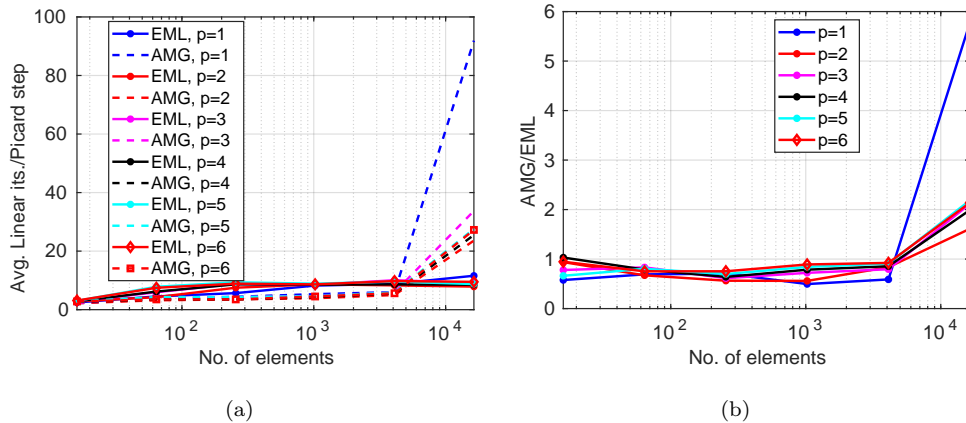


Fig. 6.12: 2D island coalescence problem: Comparison of AMG and multilevel (EML) preconditioners as the mesh is refined in h and p . In both cases we use the BFBT approximation for the inverse of the Schur complement. On the left is the number of average iterations per Picard step and on the right is the ratio of average time taken per Picard step for BFBT+AMG over BFBT+EML preconditioner.

Figure 6.12(a) shows the average number of iterations for both the AMG and the multilevel (EML) preconditioners together with the BFBT approximation for the inverse Schur complement in the block preconditioning (5.12) as the mesh and solution order are refined. In calculating this average we have omitted the iteration counts for first Picard step in the first time step. This is because the iteration counts for both EML and AMG solvers are higher for this case than the rest of the steps as we

start from a zero initial guess. Hence it is not a representative of the iteration counts taken in other time steps. Both the algorithms show almost flat iteration count until 64×64 mesh with AMG taking slightly less iteration counts than EML. However, for 128×128 mesh (last marker) and all solution orders AMG shows a sudden increase in iteration count whereas the performance of EML almost remains the same maintaining the algorithmic scalability. Thus the EML solver is more scalable than AMG in terms of mesh refinements in the settings of this experiment. Figure 6.12(b) shows the ratio of average time taken per Picard step for the BFBT+AMG preconditioner over BFBT+EML and it reflects the trend observed in the iteration counts in Figure 6.12(a). We get approximately 2 – 6 times speedup with the BFBT+EML preconditioner over BFBT+AMG preconditioner for 128×128 mesh.

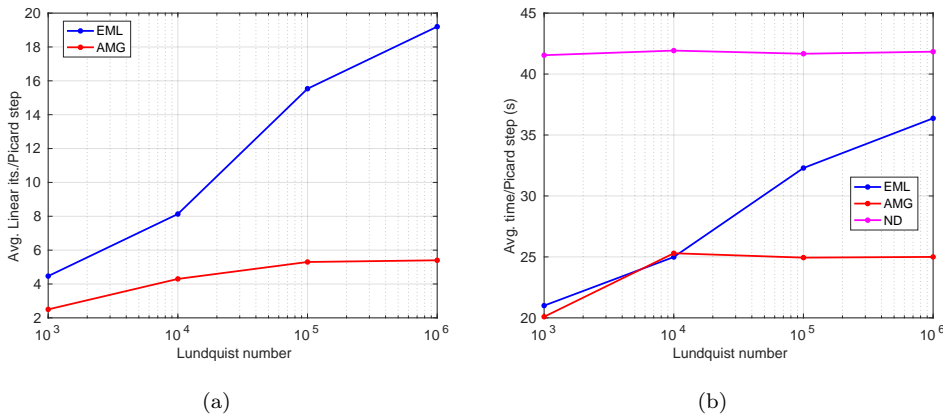


Fig. 6.13: 2D island coalescence problem: Comparison of AMG and multilevel (EML) preconditioners with increase in Lundquist number S . In both cases we use the BFBT approximation for the inverse of the Schur complement. On the left is the average iterations per Picard step and on the right is the average time taken per Picard step. We also show timings for the nested dissection (ND) direct solver on the right for comparison.

Now we test the robustness of AMG and EML preconditioners with respect to Lundquist number for this problem. To that extent we consider 64×64 , $p = 6$ mesh and choose a time stepsize of $\Delta t = 0.05$. The results are again averaged over six time steps. Figure 6.13 shows the average iteration counts and time per Picard step for Lundquist numbers in the range $[10^3, 10^6]$. We can see that the BFBT+AMG preconditioner is more robust with respect to increase in Lundquist numbers than the BFBT+EML preconditioner. Nevertheless, the growth in iterations for the BFBT+EML preconditioner is still moderate and in all the cases both the preconditioners take less time than the nested dissection (ND) direct solver. In our future work, we want to improve the robustness of the BFBT+EML preconditioner by exploring other fine scale solvers than block-Jacobi.

Finally, we will compare the BFBT+EML preconditioned GMRES with one of the fast direct solvers in 2D namely the nested dissection (ND). We use the UMF-PACK library [10] for this purpose and order the trace system matrix (5.1) in nested

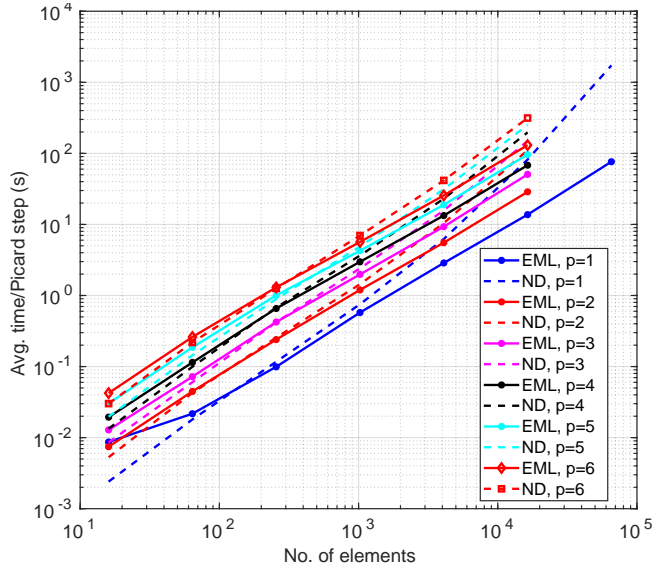


Fig. 6.14: 2D island coalescence problem: Comparison of scaling of BFBT+EML preconditioned GMRES (denoted as EML) and ND direct solver with number of elements for solution orders $p = 1 - 6$.

dissection manner. In Figure 6.14 we compare the scaling of the average time taken per Picard step with mesh refinements for the BFBT+EML preconditioned GMRES and the nested dissection direct solver for different solution orders. The dominant cost in the BFBT+EML preconditioned solver comes from the factorization involved in EML and as per the theoretical complexities derived in [26], the iterative solver at all orders show close to linear scaling with the number of elements whereas the ND direct solver shows an asymptotic scaling of $\mathcal{O}(N_T^{3/2})$.

In Figure 6.15 we show the speedup of BFBT+EML preconditioned GMRES compared to ND and we can see at all solution orders, when the number of elements is greater than 10^3 (after 5 uniform refinements) the iterative solver is faster than ND. We get a maximum speedup of approximately 23 for $p = 1$ and 256×256 elements, and the ND solver ran into out of memory issues after this. In terms of memory for $p = 1$ and 256×256 mesh, the ND solver needed 98.2 GB for the L, U factors whereas the EML part in the iterative solver needed only 2.4 GB which is 41 times less memory compared to the direct solver. This speedup and memory reduction is significantly higher than the one observed for the scalar problems studied in [26]. Thus BFBT+EML preconditioned GMRES can deliver significant speedups and memory savings compared to the ND direct solver for vector valued problems even in 2D.

7. Conclusion. In this work we present a block preconditioning strategy for the trace system coming from the HDG discretization of the incompressible resistive MHD equations. In the block preconditioner, we use least squares commutator (BFBT) approximation for the inverse of the Schur complement and a system projection AMG v-cycle for the approximate inverse of the nodal block. For the smoother inside AMG cycle, we compare preconditioned GMRES and ILU(0) smoother of overlap one and conclude that the GMRES smoother is faster, requires less memory and more robust

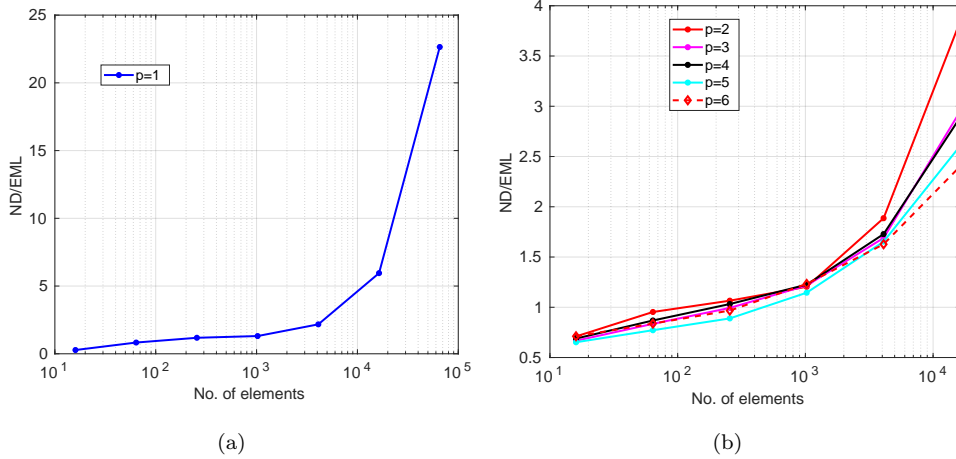


Fig. 6.15: 2D island coalescence problem: Ratio of time taken per Picard step for ND solver over BFBT+EML preconditioned GMRES for solution order $p = 1$ (left) and for orders $p = 2 - 6$ (right). The ND solver ran into out of memory issues for orders $p > 1$ and 256^2 elements.

compared to the ILU smoother. We test the performance of the block preconditioner on several 2D and 3D transient test cases including, but not limited to, the island coalescence problem at high Lundquist numbers and demonstrate robustness and parallel scalability up to thousands of cores. We also show the application of the multilevel approximate nested dissection preconditioner introduced in [26] for the approximate inverse of the nodal block and compare the performance with AMG and a full nested dissection direct solver. The BFBT+multilevel preconditioner shows better algorithmic scalability compared to BFBT+AMG with respect to mesh refinements. In terms of robustness with respect to Lundquist numbers BFBT+AMG performs better and strong smoothers are needed in the BFBT+multilevel preconditioner. In comparison with the nested dissection direct solver BFBT+multilevel preconditioned GMRES is significantly faster and requires lot less memory up to an order of magnitude.

In terms of future works improving the parallel performance and scalability of the block preconditioner is one of the primary areas of focus. This would enable large scale 3D simulation of realistic geometries that are of interest in fusion research as well as other areas of plasma physics research. Since, the block preconditioner developed here is also applicable for Stokes and incompressible Navier Stokes equations studying the performance in those contexts is also of interest.

Acknowledgements. The authors would like to thank Dr. Paul Lin for help regarding various aspects of Trilinos. SM, SS and TBT are partially supported by the Department of Energy (grant DE-SC0018147), the National Science Foundation (grants NSF-DMS1620352, Early Career NSF-OAC1808576, and NSF-OAC1750863), and the Defense Threat Reduction Agency (grant HDTRA1-18-1-0020). We are grateful for the support. At Sandia this work was partially supported by the U.S. Department of Energy, Office of Science, Office of Advanced Scientific Computing Research, Applied Mathematics Program and by the U.S. Department of Energy, Office of Sci-

ence, Office of Advanced Scientific Computing Research and Office of Fusion Energy Sciences, Scientific Discovery through the Advanced Computing (SciDAC) program. Sandia National Laboratories is a multi-mission laboratory managed and operated by National Technology and Engineering Solutions of Sandia, LLC., a wholly owned subsidiary of Honeywell International, Inc., for the U.S. Department of Energy’s National Nuclear Security Administration under contract DE-NA0003525. This paper describes objective technical results and analysis. Any subjective views or opinions that might be expressed in the paper do not necessarily represent the views of the U.S. Department of Energy or the United States Government. The authors acknowledge the Texas Advanced Computing Center (TACC) at The University of Texas at Austin for providing HPC, visualization and storage resources that have contributed to the research results reported within this paper.

REFERENCES

- [1] GIOVANNI ALZETTA, DANIEL ARNDT, WOLFGANG BANGERTH, VISHAL BODDU, BENJAMIN BRANDS, DENIS DAVYDOV, RENE GASSMÖLLER, TIMO HEISTER, LUCA HELTAI, KATHARINA KORMANN, ET AL., The deal.ii library, version 9.0, *Journal of Numerical Mathematics*, 26 (2018), pp. 173–183.
- [2] W. BANGERTH, R. HARTMANN, AND G. KANSCHAT, deal.II – a general purpose object oriented finite element library, *ACM Trans. Math. Softw.*, 33 (2007), pp. 24/1–24/27.
- [3] MICHELE BENZI, GENE H GOLUB, AND JÖRG LIESEN, Numerical solution of saddle point problems, *Acta numerica*, 14 (2005), p. 1.
- [4] A BHATTACHARJEE, YI-MIN HUANG, H YANG, AND B ROGERS, Fast reconnection in high-lundquist-number plasmas due to the plasmoid instability, *Physics of Plasmas*, 16 (2009), p. 112102.
- [5] DIETER BISKAMP, Magnetic reconnection in plasmas, *Astrophysics and Space Science*, 242 (1996), pp. 165–207.
- [6] LUIS CHACÓN, An optimal, parallel, fully implicit newton–krylov solver for three-dimensional viscoresistive magnetohydrodynamics, *Physics of Plasmas*, 15 (2008), p. 056103.
- [7] C CIUCUA, PABLO FERNANDEZ, ALEXANDRA CHRISTOPHE, NGOC CUONG NGUYEN, AND JAIME PERAIRE, Implicit hybridized discontinuous galerkin methods for compressible magnetohydrodynamics, *Journal of Computational Physics: X*, 5 (2020), p. 100042.
- [8] RAMON CODINA AND NOEL HERNÁNDEZ-SILVA, Stabilized finite element approximation of the stationary magneto-hydrodynamics equations, *Computational Mechanics*, 38 (2006), pp. 344–355.
- [9] ERIC C CYR, JOHN N SHADID, RAYMOND S TUMINARO, ROGER P PAWLOWSKI, AND LUIS CHACÓN, A new approximate block factorization preconditioner for two-dimensional incompressible (reduced) resistive MHD, *SIAM Journal on Scientific Computing*, 35 (2013), pp. B701–B730.
- [10] TIMOTHY A. DAVIS, Algorithm 832: UMFPACK V4.3—an unsymmetric-pattern multifrontal method, *ACM Transactions on Mathematical Software*, 30 (2004), pp. 196–199.
- [11] HOWARD ELMAN, VICTORIA E HOWLE, JOHN SHADID, ROBERT SHUTTLEWORTH, AND RAY TUMINARO, Block preconditioners based on approximate commutators, *SIAM Journal on Scientific Computing*, 27 (2006), pp. 1651–1668.
- [12] HOWARD C ELMAN, Preconditioning for the steady-state Navier–Stokes equations with low viscosity, *SIAM Journal on Scientific Computing*, 20 (1999), pp. 1299–1316.
- [13] HOWARD C ELMAN, DAVID J SILVESTER, AND ANDREW J WATHEN, Finite elements and fast iterative solvers: with applications in incompressible fluid dynamics, Oxford University Press, USA, 2014.
- [14] MICHAEL W GEE, CHRISTOPHER M SIEFERT, JONATHAN J HU, RAY S TUMINARO, AND MARZIO G SALA, ML 5.0 smoothed aggregation user’s guide, tech. report, Technical Report SAND2006-2649, Sandia National Laboratories, 2006.
- [15] JOHAN P GOEDBLOED, RONY KEPPENS, AND STEFAAN POEDTS, Advanced magnetohydrodynamics: with applications to laboratory and astrophysical plasmas, Cambridge University Press, 2010.
- [16] JOHAN PETER GOEDBLOED AND STEFAAN POEDTS, Principles of magnetohydrodynamics: with applications to laboratory and astrophysical plasmas, Cambridge University Press, 2004.

- [17] MICHAEL A HEROUX, ROSCOE A BARTLETT, VICKI E HOWLE, ROBERT J HOEKSTRA, JONATHAN J HU, TAMARA G KOLDA, RICHARD B LEHOUCQ, KEVIN R LONG, ROGER P PAWLOWSKI, ERIC T PHIPPS, ET AL., An overview of the trilinos project, ACM Transactions on Mathematical Software (TOMS), 31 (2005), pp. 397–423.
- [18] YI-MIN HUANG AND A BHATTACHARJEE, Scaling laws of resistive magnetohydrodynamic reconnection in the high-lundquist-number, plasmoid-unstable regime, Physics of Plasmas, 17 (2010), p. 062104.
- [19] CHRISTOPHER A KENNEDY AND MARK H CARPENTER, Diagonally implicit Runge-Kutta methods for ordinary differential equations. A review, (2016).
- [20] JEONGHUN J LEE, STEPHEN J SHANNON, TAN BUI-THANH, AND JOHN N SHADID, Analysis of an hdg method for linearized incompressible resistive mhd equations, SIAM Journal on Numerical Analysis, 57 (2019), pp. 1697–1722.
- [21] XIAOYE S LI AND JAMES W DEMMEL, SuperLU_DIST: A scalable distributed-memory sparse direct solver for unsymmetric linear systems, ACM Transactions on Mathematical Software (TOMS), 29 (2003), pp. 110–140.
- [22] PAUL LIN, JOHN N SHADID, EDWARD GEOFFREY PHILLIPS, JONATHAN J HU, ERIC C CYR, ROGER P PAWLOWSKI, ANDREY ORNL PROKOPENKO, AND PAUL LLNL TSUJI, Performance of Scalable AMG-based Preconditioners for MHD and Multifluid Plasma Simulations., tech. report, Sandia National Lab.(SNL-NM), Albuquerque, NM (United States); Sandia, 2017.
- [23] DAVE A MAY AND LOUIS MORESI, Preconditioned iterative methods for Stokes flow problems arising in computational geodynamics, Physics of the Earth and Planetary Interiors, 171 (2008), pp. 33–47.
- [24] ULRICH MÜLLER AND LEO BÜHLER, Magnetofluidynamics in Channels and Containers, Springer Science & Business Media, 2013.
- [25] SRIRAMKRISHNAN MURALIKRISHNAN, Fast and scalable solvers for high-order hybridized discontinuous Galerkin methods with applications to fluid dynamics and magnetohydrodynamics, PhD thesis, 2019.
- [26] SRIRAMKRISHNAN MURALIKRISHNAN, TAN BUI-THANH, AND JOHN N SHADID, A multilevel approach for trace system in HDG discretizations, Journal of Computational Physics, 407 (2020), p. 109240.
- [27] MALCOLM F MURPHY, GENE H GOLUB, AND ANDREW J WATHEN, A note on preconditioning for indefinite linear systems, SIAM Journal on Scientific Computing, 21 (2000), pp. 1969–1972.
- [28] EDWARD G PHILLIPS, JOHN N SHADID, ERIC C CYR, HOWARD C ELMAN, AND ROGER P PAWLOWSKI, Block preconditioners for stable mixed nodal and edge finite element representations of incompressible resistive MHD, SIAM Journal on Scientific Computing, 38 (2016), pp. B1009–B1031.
- [29] RAMON PLANAS BADENAS, Stabilized finite element formulations for solving incompressible magnetohydrodynamics, PhD thesis, 2013.
- [30] ANDREY PROKOPENKO, JONATHAN J HU, TOBIAS A WIESNER, CHRISTOPHER M SIEFERT, AND RAYMOND S TUMINARO, Muelu user’s guide 1.0, Technical Report SAND2014-18874, Sandia National Laboratories, (2014).
- [31] SANDER RHEBERGEN AND GARTH N WELLS, Preconditioning of a hybridized discontinuous Galerkin finite element method for the Stokes equations, Journal of Scientific Computing, 77 (2018), pp. 1936–1952.
- [32] JOHANN RUDI, Global convection in Earth’s mantle: advanced numerical methods and extreme-scale simulations, PhD thesis, 2019.
- [33] YOUSEF SAAD, A flexible inner-outer preconditioned GMRES algorithm, SIAM Journal on Scientific Computing, 14 (1993), pp. 461–469.
- [34] N BEN SALAH, AZZEDDINE SOULAIMANI, WAGDI G HABASHI, AND MICHEL FORTIN, A conservative stabilized finite element method for the magneto-hydrodynamic equations, International Journal for Numerical Methods in Fluids, 29 (1999), pp. 535–554.
- [35] DOMINIK SCHÖTZAU, Mixed finite element methods for stationary incompressible magneto-hydrodynamics, Numerische Mathematik, 96 (2004), pp. 771–800.
- [36] JOHN N SHADID, ROGER P PAWLOWSKI, ERIC C CYR, RAYMOND S TUMINARO, LUIS CHACÓN, AND PAULA D WEBER, Scalable implicit incompressible resistive MHD with stabilized FE and fully-coupled Newton–Krylov-AMG, Computer Methods in Applied Mechanics and Engineering, 304 (2016), pp. 1–25.
- [37] STEPHEN SHANNON, Hybridized Discontinuous Galerkin Methods for Magnetohydrodynamics, PhD thesis, 2018.
- [38] STEPHEN SHANNON, JOHN N. SHADID, TAN BUI-THANH, AND JEONGHUN J. LEE, A hybridized discontinuous Galerkin method for resistive incompressible magnetohydrodynamics, in CCR Summer Proceedings, Sandia, 2016.

- [39] BEN S SOUTHWORTH, ABDULLAH A SIVAS, AND SANDER RHEBERGEN, On fixed-point, krylov, and 2*2 block preconditioners for nonsymmetric problems, *SIAM Journal on Matrix Analysis and Applications*, 41 (2020), pp. 871–900.
- [40] PANAYOT S VASSILEVSKI, Multilevel block factorization preconditioners: Matrix-based analysis and algorithms for solving finite element equations, Springer Science & Business Media, 2008.
- [41] MICHAEL WATHEN AND CHEN GREIF, A scalable approximate inverse block preconditioner for an incompressible magnetohydrodynamics model problem, *SIAM Journal on Scientific Computing*, 42 (2020), pp. B57–B79.
- [42] MICHAEL WATHEN, CHEN GREIF, AND DOMINIK SCHOTZAU, Preconditioners for mixed finite element discretizations of incompressible mhd equations, *SIAM Journal on Scientific Computing*, 39 (2017), pp. A2993–A3013.
- [43] MICHAEL P WATHEN, Preconditioners for incompressible magnetohydrodynamics, PhD thesis, University of British Columbia, 2018.